



# The Global Crust and Mantle Gravity Disturbances and Their Implications on Mantle Structure and Dynamics

Bo Chen<sup>1,2</sup> · Mikhail K. Kaban<sup>3</sup> · Guangdong Zhao<sup>4</sup> · Jinsong Du<sup>5</sup> · Dawei Gao<sup>1,2</sup>

Received: 19 December 2022 / Accepted: 25 September 2023 / Published online: 4 November 2023  
© The Author(s), under exclusive licence to Springer Nature B.V. 2023

## Abstract

The gravity anomalies reflect density perturbations at different depths, which control the physical state and dynamics of the lithosphere and sub-lithospheric mantle. However, the gravity effect of the crust masks the mantle signals. In this study, we develop two frameworks (correction with density contrasts and actual densities) to calculate the gravity anomalies generated by the layered crust. We apply the proposed approaches to evaluate the global mantle gravity disturbances based on the new crustal models. Consistent patterns and an increasing linear trend of the mantle gravity disturbances with lithospheric thickness and  $V_s$  velocities at 150 km depth are obtained. Our results indicate denser lithospheric roots in most cratons and lighter materials in the oceanic mantle. Furthermore, our gravity map corresponds well to regional geological features, providing new insights into mantle structure and dynamics. Specifically, (1) reduced anomalies associated with the Superior and Rae cratons indicate more depleted roots compared with other cratons of North America. (2) Negative anomalies along the Cordillera (western North America) suggest mass deficits owing to the buoyant hot mantle. (3) Positive anomalies in the Baltic, East European, and Siberian cratons support thick, dense lithosphere with significant density heterogeneities, which could result from thermo-chemical modifications of the cratonic roots. (4) Pronounced positive anomalies correspond to stable blocks, e.g., Arabian Platform, Indian Craton, and Tarim basin, indicating a thick, dense lithosphere. (5) Low anomalies in the active tectonic units and back-arc basins suggest local mantle upwellings. (6) The cold subducting/detached plates may result in the high anomalies observed in the Zagros and Tibet.

**Keywords** Forward calculation · Tesseroids · Mantle gravity disturbance · Mantle dynamics

## Article Highlights

- Two frameworks are developed for forward calculations of the mantle gravity disturbances using new sedimentary and crustal models
- The mantle gravity disturbances imply denser lithospheric roots in most cratons and lighter materials in the oceanic mantle
- The mantle disturbances correspond well to regional geological features, providing new insights into mantle structure and dynamics

## 1 Introduction

Gravity data show a direct effect of the density heterogeneities of the Earth's interior. Many studies were carried out based on the observed gravity field, geoid, and gravity gradients to infer subsurface structure or to detect density variations in the crust or upper mantle (Deng et al. 2017, 2014; Kaban et al. 2015; Ke et al. 2019; Liang et al. 2019; Root et al. 2017; Zhao et al. 2021; Zhong et al. 2022). The mantle density variation is crucial for understanding mantle dynamics and controls tectonic processes and surface deformation (Mooney and Kaban 2010). The mantle gravity anomalies are the primary input for estimating mantle density perturbations. Since the observed gravity field is generated by the density heterogeneities of the entire Earth, it is difficult to separate the gravity signal caused by the density anomalies in the mantle without prior information. In particular, the crust is the most heterogeneous layer inside the Earth, and its gravity signal overshadows the signals of other layers, especially on a regional level (Kaban et al. 2003, 2016b). Therefore, it is necessary to remove the contaminating effect of the crust to better image the underlying mantle (Herceg et al. 2016; Kaban et al. 2003; Tenzer and Chen 2019; Tenzer et al. 2009). The quality of the obtained results directly depends on the crustal models, which are continuously improved. Consequently, the residual mantle anomalies should also be recalculated from time to time.

The stripping technique is one of the most common ways to calculate mantle anomalies. The crustal gravity effect is calculated based on an a priori crustal model mainly defined by seismic studies and subsequently subtracted from the observed Bouguer gravity field (Herceg et al. 2016; Kaban et al. 2003, 2010). As a result, the main assumption is that the residual gravity anomalies directly image density variations in the mantle. Several attempts have been made to calculate mantle gravity anomalies on regional and global scales. For the regional studies, Artemjev et al. (1994) obtained the mantle gravity anomalies for Northern Eurasia. However, they did not consider the gravity effect of the density structure of the crystalline crust. Mooney and Kaban (2010) presented an integrated mantle gravity map of North America by subtracting the gravitational contributions of topography, sedimentary accumulations, and the crystalline crust determined by seismic observations. Additionally, the regional mantle disturbance maps for Europe (Kaban et al. 2010), the Middle East (Kaban et al. 2016a), Asia (Kaban et al. 2016b), the Siberian craton (Artemieva et al. 2019), and the European-North Atlantic region (Shulgin and Artemieva 2019) were estimated based on regional crustal models. These maps have been used to study the density structures of the upper mantle on a regional scale. Since these studies presented the regional mantle gravity maps using different crustal models and reference frames, the mantle gravity anomalies in different areas cannot be compared directly, and therefore, it is hard to provide insights into the global tectonics and mantle dynamics.

For global studies, Kaban et al. (1999) presented the first residual crust-free gravity field truncated after degree 20 based on the CRUST5.1 model (Mooney et al. 1998). An improved next-generation map of the residual mantle gravity anomalies was calculated using the CRUST2.0 model by Kaban et al. (2003). These two earlier low-resolution mantle gravity fields were computed using the coarsely constrained global crustal models, which are now largely outdated. Most of the aforementioned regional and global calculations were carried out in the spatial domain, considering the sphericity of the Earth, but a detailed process for the calculations was not usually presented in these studies. Later, Tenzer et al. (2009) developed global maps of the complete crust-stripped (relative to the mantle) gravity disturbances at the Earth's surface based on the EGM2008 geopotential model and the CRUST2.0 crustal model using spherical harmonic analysis. Subsequently, the mantle gravity maps were refined using the CRUST1.0 model (Tenzer et al. 2015) and the LITHO1.0 lithospheric model (Tenzer and Chen 2019) based on the same spectral method. However, there are significant differences in amplitudes and regional patterns among the global mantle gravity anomalies obtained by different studies in the spatial and spectral domains.

It is well known that the forward modeling method based on spherical harmonic analysis is suitable for global calculations, while it is not applicable for calculating the gravity field in regional studies. Moreover, the accuracy of the spectral forward calculation using spherical harmonic analysis decreases with the increasing depth of the calculation layer due to the truncation of the binomial series (Root et al. 2016). In contrast, spatial forward modeling is applicable for the forward calculations of gravity anomalies at both global and regional levels. When tackling large-scale problems, the forward analysis of the gravity field has been commonly developed in spherical coordinates based on the tesseroid (spherical prism) subdivision to consider the curvature of the Earth (Asgharzadeh et al. 2007; Gómez-García et al. 2019; Grombein et al. 2013; Heck and Seitz 2007; Wild-Pfeiffer 2008). These spatial forward methods have been widely used for terrain correction and gravity inversion on regional and global scales (Grombein et al. 2016; Liang et al. 2014; Zhao et al. 2019, 2021). Recently, Uieda et al. (2016) developed the open-source software named Tesseroids using the Gauss–Legendre quadrature (GLQ) with an adaptive discretization algorithm, significantly improving the accuracy of the forward calculation in spherical coordinates. These methods based on a subdivision of tesseroids will be taken as a basis for this study.

In this study, we first clarify the process of obtaining mantle gravity anomalies and develop two approaches for calculating mantle gravity anomalies in the spatial domain. Subsequently, these methods are used to evaluate the gravity disturbances reflecting the mantle gravity signals on a global scale based on recent crustal models. Finally, we discuss the implications of the resulting mantle gravity maps for the structure and dynamics on global and continental scales.

## 2 Forward Gravity Modeling and Crustal Gravity Corrections

For current available global crustal models (e.g., CRUST2.0, CRUST1.0, LITHO1.0) and most regional crustal models, the crust is commonly divided into several layers, including the topographic masses, sedimentary and crystalline crust layers, and Moho

undulations. For the layered-based crustal models, the density (or velocity) varies laterally in each layer, but it is constant in the vertical direction. In this study, to consider the curvature of the Earth, 3-D forward modeling on the spatial domain using tesseroid mass bodies, as introduced by Anderson (1976), is applied to calculate the disturbing gravity of each layer within the crust.

### 2.1 Forward Modeling with Tesseroids

As illustrated in Fig. 1, a layered body is decomposed into  $N'_\lambda$  and  $N'_\varphi$  segments with equal mesh intervals of  $\Delta\lambda$  and  $\Delta\varphi$  in the longitudinal and latitudinal directions, respectively, defining a total tesseroid number of  $N'_\lambda \times N'_\varphi$ . For each tesseroid, its geometrical center is  $(r', \varphi'_n, \lambda'_m)$ , where  $n = 1, 2, 3, \dots, N'_\varphi$ ;  $m = 1, 2, 3, \dots, N'_\lambda$ . The radial dimension  $\Delta r$  is defined by the thickness of the layer,  $r'$  is the geocentric radius of each tesseroid  $(n, m)$ , and they are defined as:

$$\begin{aligned} \Delta r &= |bd_1 - bd_2|, \\ r' &= R_0 + \frac{bd_1 + bd_2}{2}, \end{aligned} \tag{1}$$

where  $R_0$  is the reference surface radius;  $bd_1$  and  $bd_2$  ( $bd_1 \geq bd_2$ ) are the upper and lower boundary surfaces of the layer at the location  $(\varphi'_n, \lambda'_m)$ , which are positive upward, and equal to zero at the reference surface radius.

The vertical gradient of the gravitational potential (i.e., the gravitational accelerations in the radius direction) at the computation point  $P(r, \varphi, \lambda)$  due to the tesseroid  $(n, m)$  with a specific mass density is evaluated by (Grombein et al. 2013; Uieda et al. 2016; Zhao et al. 2019),

$$g_{nm}(r, \varphi, \lambda) = G\rho(\varphi'_n, \lambda'_m) \int_{r'-0.5\Delta r}^{r'+0.5\Delta r} \int_{\lambda'_m-0.5\Delta\lambda}^{\lambda'_m+0.5\Delta\lambda} \int_{\varphi'_n-0.5\Delta\varphi}^{\varphi'_n+0.5\Delta\varphi} \frac{r' \cos\psi - r}{\ell^3} r'^2 \cos\varphi' dr' d\varphi' d\lambda', \tag{2}$$

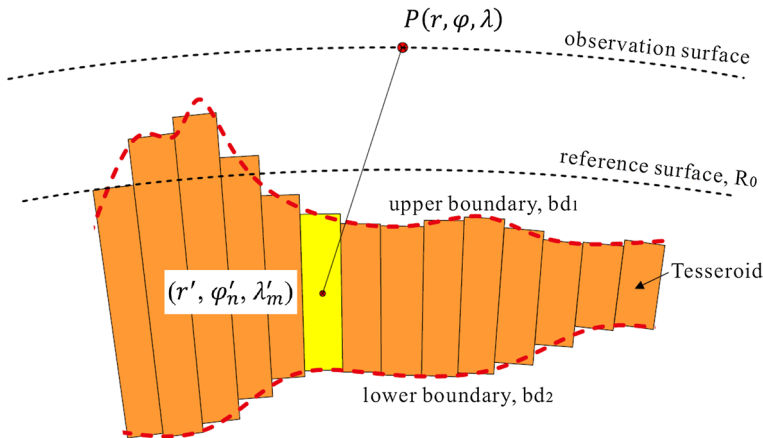


**Fig. 1** Discretization of the layer within the Earth with tesseroids.  $bd_1$  and  $bd_2$  represent the upper and lower boundaries of the layer, respectively.  $P(r, \varphi, \lambda)$  is the computation point,  $(r', \varphi'_n, \lambda'_m)$  represents the geometrical center of the calculated tesseroid, and  $R_0$  is the reference surface radius



$$\begin{aligned} \ell &= \sqrt{r'^2 + r^2 - 2r'r \cos \psi}, \\ \cos \psi &= \sin \varphi \sin \varphi' + \cos \varphi \cos \varphi' \cos (\lambda' - \lambda). \end{aligned}$$

Here  $G$  is the gravitational constant,  $\rho(\varphi'_n, \lambda'_m)$  is the density of the tesseroid bounded by a pair of concentric spheres ( $r' - 0.5\Delta r, r' + 0.5\Delta r$ ), meridional planes ( $\lambda'_m - 0.5\Delta\lambda, \lambda'_m + 0.5\Delta\lambda$ ), and coaxial circular cones defined by parallels ( $\varphi'_n - 0.5\Delta\varphi, \varphi'_n + 0.5\Delta\varphi$ ).

Based on the superposition principle, the disturbing gravity  $g(r, \varphi, \lambda)$  generated by a specific layer at the observation point is the sum of the contributions from all the tesseroids:

$$g(r, \varphi, \lambda) = \sum_{m=1}^{N'_\lambda} \sum_{n=1}^{N'_\varphi} g_{nm}(r, \varphi, \lambda), \tag{3}$$

The 3-D Gauss–Legendre quadrature (GLQ) algorithm (Asgharzadeh et al. 2007) with a GLQ order of four is applied here for all three dimensions. In addition, the adaptive discretization strategy (Uieda et al. 2016) is employed to ensure high accuracy, in which any initial tesseroid is sub-discretized into small tesseroids iteratively using the predefined criterion of the distance-size ratio  $D=1.5$  (Uieda et al. 2016). A homogenous spherical shell with a density of  $2670 \text{ kg/m}^3$  and a thickness of 1 km ranging from 6371 to 6372 km is employed for accuracy estimation. We divide the shell into regular tesseroids with the size  $1^\circ \times 1^\circ$ . Comparing the computed tesseroids effects with the analytical solution of the shell at 1 km height indicates that the maximum relative error of the tesseroids calculations is about 0.002%.

### 2.2 Earth’s Gravity Disturbances and Topographic Mass Corrections

Here, we analyze the observed gravity field in terms of the gravity disturbances (Hofmann-Wellenhof and Moritz 2006). The spherical approximation of the free-air gravity disturbances  $\Delta g_{FA}$  (i.e., the negative radial derivative of the disturbing potential) are calculated using the spherical harmonic expansion, e.g., Barthelmes (2013):

$$\Delta g_{FA}(r, \varphi, \lambda) = \frac{GM}{r^2} \sum_{l=0}^{l_{max}} \sum_{m=0}^l \left(\frac{R}{r}\right)^l (l+1) (C_{lm}^T \cos m\lambda + S_{lm}^T \sin m\lambda) P_{lm}(\sin\varphi), \tag{4}$$

where  $(r, \varphi, \lambda)$  are the coordinates of observation points;  $R$  is the reference radius;  $GM$  is the gravitational constant times the mass of the Earth;  $l$  is the degree,  $m$  is the order;  $C_{lm}^T$  and  $S_{lm}^T$  are the normalized spherical harmonic coefficients of degree  $l$  and order  $m$  for the disturbing potential;  $P_{lm}$  is the fully normalized associated Legendre function. The coefficients  $(C_{lm}^T, S_{lm}^T)$  of the disturbing potential are obtained by

$$C_{lm}^T = C_{lm}^W - C_{lm}^U, S_{lm}^T = S_{lm}^W - S_{lm}^U, \tag{5}$$

where  $(C_{lm}^W, S_{lm}^W)$  and  $(C_{lm}^U, S_{lm}^U)$  are the fully normalized Stokes’ coefficients of the observed gravity field and the normal potential, respectively. In general, the expansion of the normal ellipsoidal potential contains only the terms for the order  $m=0$  and degrees  $l=\text{even}$ . Thus, the normal potential can be determined by the first few zonal harmonic coefficients, such as  $C_{00}^U, C_{20}^U, C_{40}^U, C_{60}^U$  and  $C_{80}^U$  (Barthelmes 2013). For details on the formulas of the normal potential coefficients, refer to Hofmann-Wellenhof and Moritz (2006).

The gravity effect of the topography/bathymetry variation near the surface is a significant component of the gravity disturbances. The topographic mass corrections are generally

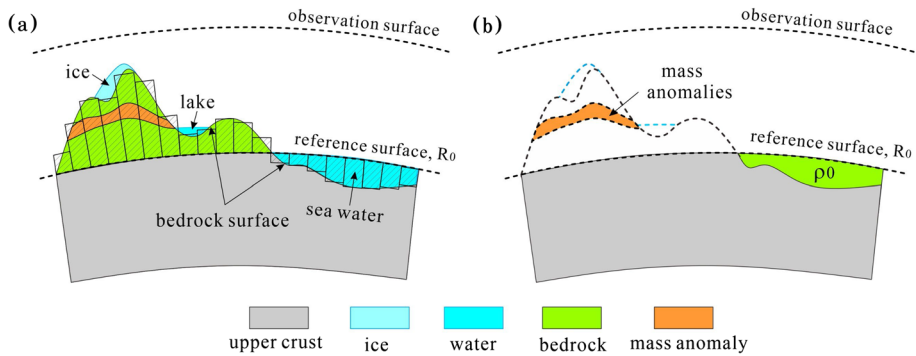


**Fig. 2** **a** Schematic representation of the topographic masses before correction and the discretization of the bedrock, **b** the mass distribution after the topographic mass correction.  $\rho_0$  is the density used in the topographic bedrock correction ( $\rho_0=2670 \text{ kg/m}^3$  in this study). The mass anomaly is defined as the residual mass with density contrast ( $\rho - \rho_0$ ), which is located above the reference surface with a density ( $\rho$ ) different from the specific density value ( $\rho_0$ ) of the terrain correction, e.g.,  $\rho \neq \rho_0$

carried out to get the Bouguer gravity disturbances, which reflect subsurface density variations. The topographic masses encompass land topography, oceans, lakes, and ice masses. Following the Rock–Water–Ice (RWI) approach proposed by Grombein et al. (2014, 2016), the gravity effect of the topographic masses  $\delta g_{TC}$  combines the gravity signals of the bedrock  $\delta g_{bed}$ , water  $\delta g_{water}$ , and ice  $\delta g_{ice}$  with corresponding density values,

$$\delta g_{TC} = \delta g_{ice} + \delta g_{water} + \delta g_{bed}, \tag{6}$$

where  $\delta g_{ice}$ , and  $\delta g_{water}$  can be computed using the forward approach presented in Sect. 2.1. For the calculation of  $\delta g_{bed}$ , the upper and lower boundary surfaces of the rock mass are defined by the bedrock topography/bathymetry, and the reference surface radius  $R_0$  globally as shown in Fig. 2a.

By reducing the attraction of the Earth’s topographic masses from the free-air gravity disturbances  $\Delta g_{FA}$ , we obtain the Bouguer gravity disturbances  $\Delta g_{BG}$ ,

$$\Delta g_{BG} = \Delta g_{FA} - \delta g_{TC}. \tag{7}$$

It is worth mentioning that for the masses located above the reference surface with a density different from the specific density value of the terrain correction (e.g.,  $\rho_0=2670 \text{ kg/m}^3$  in this study), their residual gravity effects remain in the Bouguer gravity disturbances, such as the mass anomalies shown in Fig. 2b. After the topographic mass corrections, most of the masses above the reference surface are removed. The mass defects below the reference surface are supplemented with the reference density ( $\rho_0$ ), such as in marine areas, as shown in Fig. 2b.

In the following sections, we develop two different frameworks for the layer-based forward computations with density contrasts or actual layer densities in the spatial domain to account for the crustal gravity contribution and to obtain the mantle gravity disturbances.

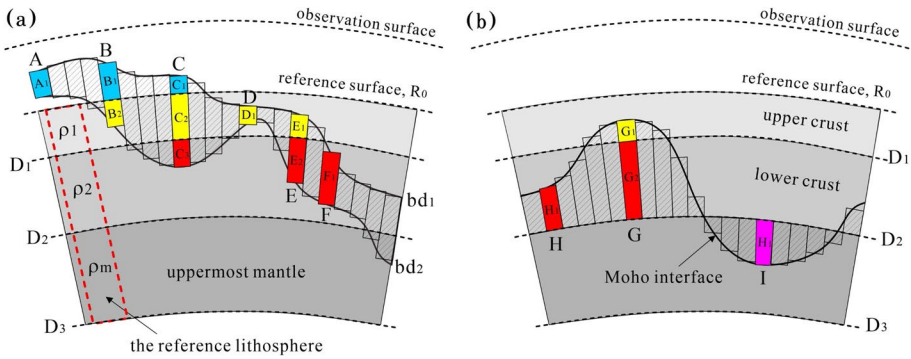


**Fig. 3** Schematic representation of the reference model and the subdivision cases of **a** the crustal layer, and **b** the Moho variations. The alphabets A-I represent the subdivision cases in Table 2

**Table 1** Parameters of the three-layer reference model and topographic mass correction

Parameters	Symbol	Values
Upper crust depth (km) <sup>a</sup>	$D_1$	-15
Lower crust depth (km) <sup>a</sup>	$D_2$	-40
Uppermost mantle depth (km) <sup>a</sup>	$D_3$	-75
Upper crust density (kg/m <sup>3</sup> ) <sup>a</sup>	$\rho_1$	2700
Lower crust density (kg/m <sup>3</sup> ) <sup>a</sup>	$\rho_2$	2940
Uppermost mantle density (kg/m <sup>3</sup> ) <sup>a</sup>	$\rho_m$	3300
Average topographic density (kg/m <sup>3</sup> ) <sup>b</sup>	$\rho_0$	2670
Density of the ice layer (kg/m <sup>3</sup> ) <sup>b</sup>	$\rho_{ice}$	920
Density of the seawater (kg/m <sup>3</sup> ) <sup>b</sup>	$\rho_w$	1020

<sup>a</sup>Parameters of the reference model

<sup>b</sup>Parameters for topographic mass correction

### 2.3 Crustal Layer Corrections Using Density Contrast

As mentioned before, the Bouguer gravity field reflects the gravity effect caused by all density contrasts within the Earth with respect to a standard density distribution inside the reference ellipsoid, which generates the normal gravity field (Tenzer et al. 2009; Vajda et al. 2008). To estimate the gravity signals of the density heterogeneities within the crust, a reference lithospheric density model depending on depth is usually predefined as the background density distribution (Kaban et al. 2003; Mooney and Kaban 2010; Tenzer et al. 2009).

A laterally homogeneous three-layer model is defined here as the reference lithosphere in this study (Fig. 3a), which has zero topography at the surface. The upper crust ranges from the surface down to the depth  $D_1$  and has a density  $\rho_1$ , the lower crust down to the depth  $D_2$  with density  $\rho_2$ , and the uppermost mantle down to  $D_3$  (deeper than the maximum Moho) with density  $\rho_m$ . The gravity corrections of the entire crust are estimated relative to this reference density model. The specific values used for this correction are presented in Table 1.

The crust commonly consists of several sedimentary and crystalline crust layers. The gravity correction of the crust combines the effects from both the sedimentary ( $\delta g_{\text{sed}}$ ) and crystalline crustal layers ( $\delta g_{\text{crust}}$ ). We apply these two corrections ( $\delta g_{\text{sed}} + \delta g_{\text{crust}}$ ) to the Bouguer gravity disturbances, getting the so-called crust-stripped gravity disturbances (Tenzer et al. 2009). The gravity effect of each sedimentary and crystalline crustal layer is calculated using the algorithm presented in Sect. 2.1. Since the gravity anomalies of the crust are evaluated relative to the reference model, the density contrasts of each layer become variable along the depth rather than constant.

To account for the varying density in the vertical direction, the elementary mass body at each grid is subdivided into sub-tesseroids with a constant density. As shown in Fig. 3, the subdivision is based on the layer boundary surfaces (i.e.,  $bd_1$  and  $bd_2$ ) relative to the reference depths  $D_1$  and  $D_2$ . This scheme can achieve high computation accuracy in combination with the adaptive discretization strategy of tesseroids (Uieda et al. 2016). There are six cases for the three-layer reference model (cases A–F), and a schematic representation of the mass discretization of one possible crustal layer is shown in Fig. 3a. At each location, the maximum number of the sub-tesseroids is three (case C). The sub-tesseroids at each grid have the same horizontal dimensions but different radial dimensions, geocentric radii, and density contrasts. Table 2 presents the parameters of the sub-tesseroids for all six cases relative to the three-layer reference crust. For example, a crustal layer with  $bd_1$  and  $bd_2$  above the reference surface  $R_0$  (i.e.,  $bd_1 \geq bd_2 \geq 0$ , case A), and the mass at that location can be represented by one tesseroid with the density ( $\rho - \rho_0$ ) and no subdivision is needed, where  $\rho$  is the location-dependent density of the calculation layer. If  $bd_1 > 0$  and the lower boundary of the layer  $bd_2$  is below the

**Table 2** The subdivision cases of the layered lithospheric masses with respect to the three-layer reference model in the correction scheme using density contrast

Case	Layer boundary condition	Sub-tesseroid number	Radial dimension ( $\Delta r$ )	Geocentric radius ( $r'$ )	Density contrast
A	$bd_1 \geq bd_2 \geq 0$	A <sub>1</sub>	$bd_1 - bd_2$	$R_0 + (bd_1 + bd_2)/2$	$\rho - \rho_0$
B	$bd_1 \geq 0 \geq bd_2 > D_1$	B <sub>1</sub>	$bd_1$	$R_0 + bd_1/2$	$\rho - \rho_0$
		B <sub>2</sub>	$-bd_2$	$R_0 + bd_2/2$	$\rho - \rho_1$
C	$bd_1 \geq 0, D_1 \geq bd_2$	C <sub>1</sub>	$bd_1$	$R_0 + bd_1/2$	$\rho - \rho_0$
		C <sub>2</sub>	$-D_1$	$R_0 + D_1/2$	$\rho - \rho_1$
		C <sub>3</sub>	$D_1 - bd_2$	$R_0 + (D_1 + bd_2)/2$	$\rho - \rho_2$
D	$0 \geq bd_1 \geq bd_2 \geq D_1$	D <sub>1</sub>	$bd_1 - bd_2$	$R_0 + (bd_1 + bd_2)/2$	$\rho - \rho_1$
E	$0 \geq bd_1 \geq D_1 \geq bd_2$	E <sub>1</sub>	$bd_1 - D_1$	$R_0 + (D_1 + bd_1)/2$	$\rho - \rho_1$
		E <sub>2</sub>	$D_1 - bd_2$	$R_0 + (D_1 + bd_2)/2$	$\rho - \rho_2$
F	$D_1 \geq bd_1 \geq bd_2$	F <sub>1</sub>	$bd_1 - bd_2$	$R_0 + (bd_1 + bd_2)/2$	$\rho - \rho_2$
G	$bd_1 \geq D_1$	G <sub>1</sub>	$bd_1 - D_1$	$R_0 + (D_1 + bd_1)/2$	$\rho_m - \rho_1$
		G <sub>2</sub>	$D_1 - bd_2$	$R_0 + (D_1 + bd_2)/2$	$\rho_m - \rho_2$
H	$D_1 > bd_1 \geq D_2$	H <sub>1</sub>	$bd_1 - bd_2$	$R_0 + (bd_1 + bd_2)/2$	$\rho_m - \rho_2$
		I <sub>1</sub>	$bd_2 - bd_1$	$R_0 + (bd_1 + bd_2)/2$	$\rho_2 - \rho_m$

$bd_1$  and  $bd_2$  represent the upper and lower boundary of the sedimental and crustal layers.  $D_1, D_2, \rho_0, \rho_1, \rho_2, \rho_m$  are defined by the reference lithosphere (Fig. 3a and Table 1).  $R_0$  is the reference surface radius.  $\rho$  is the location-dependent density of the calculation layer. A–F indicate the subdivision cases for the sedimental and crustal layers. G–I correspond to the subdivision cases of the Moho mass

reference surface but shallower than  $D_1$  ( $bd_1 \geq 0 \geq bd_2 > D_1$ , case B), the mass layer at this grid is subdivided into two sub-tesseroids, with the densities  $(\rho - \rho_0)$  (the blue bar  $B_1$ ) and  $(\rho - \rho_1)$  (the yellow bar  $B_2$ ) in Fig. 3a. For the case C ( $bd_1 \geq 0, D_1 \geq bd_2$ ), three sub-tesseroids with the densities  $(\rho - \rho_0)$  (the blue bar  $C_1$ ),  $(\rho - \rho_1)$  (the yellow bar  $C_2$ ) and  $(\rho - \rho_2)$  (the red bar  $C_3$ ) are implemented. The codes that reproduce the gravity effect of one crustal layer are available in Chen et al. (2022).

To further reveal the gravity signals of the mantle, the gravity effect of the Moho interface ( $\delta g_{\text{Moho}}$ ) is required to be corrected because it is one of the most prominent density boundaries inside the Earth. Likewise, we utilize mass discretization, as shown in Fig. 3b, to compute the gravity response of the Moho with respect to the reference lithosphere. For Moho depths shallower than the reference depth  $D_1$  (case G), the mass at that location is subdivided into two sub-tesseroids, with densities  $(\rho_m - \rho_1)$  (yellow bar in Fig. 3b) and  $(\rho_m - \rho_2)$  (red bar in Fig. 3b), respectively. The parameters of the sub-tesseroids for different boundary conditions are given in Table 2 (Cases G–I).

By summing up these three fields, we obtain the total crustal gravity effect  $\delta g_{\text{cs1}}$  generated by the sediments, crystalline crust, and Moho variation relative to the reference model,

$$\delta g_{\text{cs1}} = \delta g_{\text{sed}} + \delta g_{\text{crust}} + \delta g_{\text{Moho}}, \tag{8}$$

Correcting the total crustal gravity effect from the Bouguer gravity disturbances, we obtain the mantle gravity disturbances. Note that the density of the bedrock correction  $\rho_0$  is commonly set to  $2670 \text{ kg/m}^3$  in most previous studies (e.g., Claessens and Hirt 2013; Grombein et al. 2016; Hirt et al. 2019; Rexer et al. 2016), which is often different from  $\rho_1$  corresponding to the reference model, for example,  $\rho_1 = 2700 \text{ kg/m}^3$  in this study. When the bedrock surface is below the reference surface (such as in marine areas), the compensated mass with density  $(\rho_0)$  by the bedrock correction is slightly less than the upper crust ( $\rho_1$ ) of the reference crust, which affects the calculated gravity fields. Hence, the gravity effect ( $\delta g_{\text{bc}}$ ) of this mass discrepancy (Fig. 2b) is required to be compensated with the density contrast  $(\rho_1 - \rho_0) \text{ kg/m}^3$ .

Finally, the sediment-stripped gravity disturbances  $\Delta g_{\text{ss}}$ , crust-stripped gravity disturbances  $\Delta g_{\text{cs1}}$  and mantle gravity disturbances  $\Delta g_{\text{m1}}$  are expressed by,

$$\Delta g_{\text{ss}} = \Delta g_{\text{BG}} - \delta g_{\text{sed}} + \delta g_{\text{bc}}, \tag{9}$$

$$\Delta g_{\text{cs}} = \Delta g_{\text{BG}} - \delta g_{\text{sed}} - \delta g_{\text{crust}} + \delta g_{\text{bc}}, \tag{10}$$

$$\Delta g_{\text{m1}} = \Delta g_{\text{BG}} - \delta g_{\text{cs1}} + \delta g_{\text{bc}}. \tag{11}$$

If  $\rho_0 = \rho_1, \delta g_{\text{bc}} = 0$ . When  $\rho_0 \neq \rho_1$ , the upper boundary for the calculation of  $\delta g_{\text{bc}}$  is defined by the reference surface, and the lower boundary is constrained by the bathymetry.

## 2.4 Crustal Corrections with Actual Densities

Calculating the gravity effect of all layers based on their actual densities is an alternative method to account for the contribution of the crust (Herceg et al. 2016). The crustal correction  $\delta g_{\text{cc}}$  is calculated as the difference between the gravity signals of the true crustal layers and the reference model, i.e.,

$$\delta g_{\text{cc}} = g_{\text{sed}} + g_{\text{crust}} + g_{\text{Moho}} - g_{\text{ref}}, \tag{12}$$

where  $g_{\text{sed}}$ ,  $g_{\text{crust}}$ ,  $g_{\text{Moho}}$  are the gravity effects generated by the sedimentary layers, crystalline crust layers, and Moho variations, respectively, with their actual densities. The gravity value of the reference density model  $g_{\text{ref}}$  is computed by summing the gravity effects of the three reference layers (Table 1).

Likewise, each layer is discretized into a regular mesh along the horizontal dimensions as in Sect. 2.3, and its gravity effect is calculated using the forward algorithm introduced in Sect. 2.1. The radial size and geocentric radius of each cell are determined by the upper and lower boundary surface using Eq. (1). Since the actual densities of each layer are assumed constant along the depth, a subdivision strategy (as presented in Sect. 2.3) is not required in this calculation. For the calculation of  $g_{\text{Moho}}$ , the masses above the Moho have already been considered in the crust effect ( $g_{\text{crust}}$ ), hence, only the masses below the Moho (i.e., uppermost mantle) must be considered for the gravity effect of Moho variations. Therefore, the Moho layer is defined as the mass volume extending from the Moho (as the upper boundary) to the depth  $D_3$  (as the lower boundary, Table 1) with density  $\rho_m$ .

It is worth noting that the sum of the three effects ( $g_{\text{sed}} + g_{\text{crust}} + g_{\text{Moho}}$ ) corresponds to the total gravity effect of the lithosphere with topography variations at the Earth's surface and the uppermost mantle down to  $D_3$ . Since the reference model has zero topography at the surface, the correction  $\delta g_{\text{total}}$  also includes the gravity effect generated by the topography/bathymetry (i.e., bedrock), which is already considered in the topographic mass correction. In comparison with  $\delta g_{\text{cs1}}$ , the gravity effect of the bedrock ( $\delta g_{\text{bed}} - \delta g_{\text{bc}}$ ) is needed to be removed from the correction  $\delta g_{\text{total}}$ . As a result, the crustal gravity anomalies  $\delta g_{\text{cs2}}$  are evaluated by

$$\begin{aligned}\delta g_{\text{cs2}} &= \delta g_{\text{cc}} - (\delta g_{\text{bed}} - \delta g_{\text{bc}}) \\ &= g_{\text{sed}} + g_{\text{crust}} + g_{\text{Moho}} - g_{\text{ref}} - \delta g_{\text{bed}} + \delta g_{\text{bc}}.\end{aligned}\quad (13)$$

Finally, after removing the crustal correction  $\delta g_{\text{cs2}}$  from the Bouguer gravity disturbances  $\Delta g_{\text{BG}}$ , we obtain the mantle gravity disturbances  $\Delta g_{\text{m2}}$  based on the actual densities as:

$$\begin{aligned}\Delta g_{\text{m2}} &= \Delta g_{\text{BG}} - \delta g_{\text{cs2}} + \delta g_{\text{bc}} \\ &= \Delta g_{\text{BG}} - \delta g_{\text{cc}} + \delta g_{\text{bed}}.\end{aligned}\quad (14)$$

It is worth noting that a change in the reference model would lead to a shift in the average level of the computed mantle gravity field. Therefore, the resulting mantle gravity disturbances are obtained by setting the mean value of the field to 0 since the absolute value depends on the choice of the reference model (Kaban et al. 2016b; Mooney and Kaban 2010; Shulgin and Artemieva 2019).

### 3 Data and Results

In this study, we utilize recent crustal models to evaluate the gravity effects of density heterogeneities in the crust. For the continents, the thickness and density model of sediments is based on the recent regional studies for Europe (Kaban et al. 2010), Asia (Kaban et al. 2016b; Stolk et al. 2013), North America (Mooney and Kaban 2010), Antarctica (Haeger et al. 2019), Australia (Tesauro et al. 2020), South America (Finger et al. 2021), and Africa (Finger et al. 2022). For the marine areas, we employ the high-resolution model (GlobSed) of the sedimentary thickness (Straume et al. 2019). The typical density-depth relationship



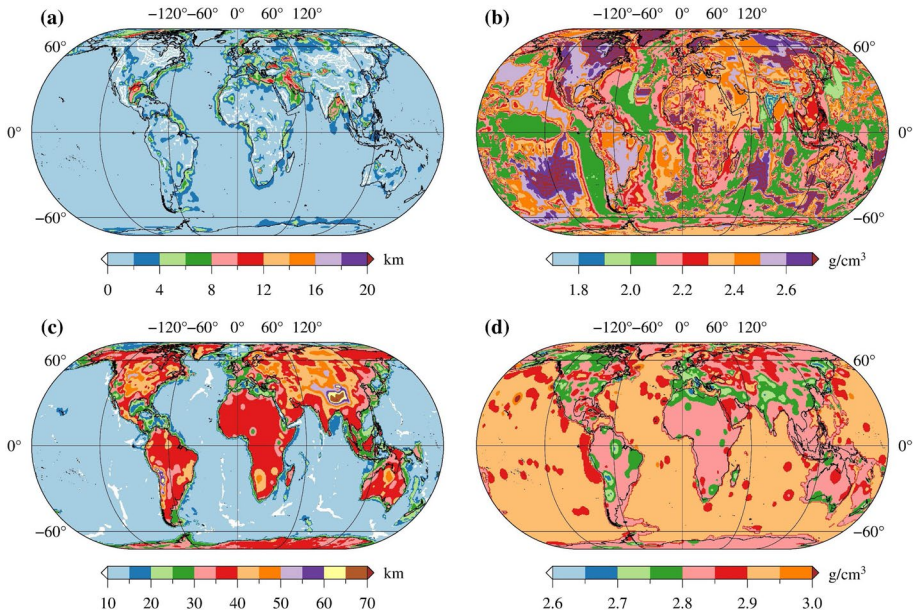


**Fig. 4** Maps of **a** the thickness and **b** the average density of the sediments, **c** the Moho depth, and **d** the mean crustal density

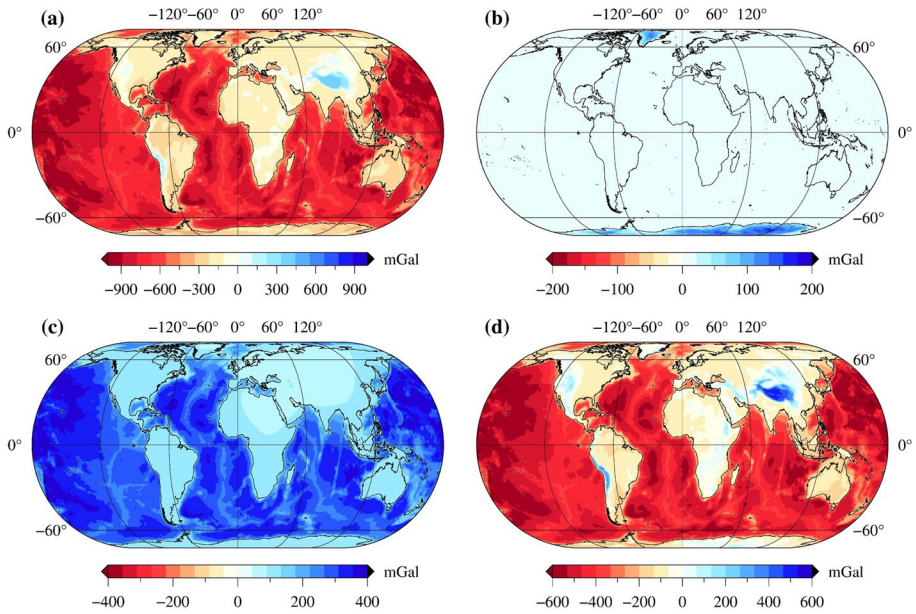


**Fig. 5** The gravity effects of **a** the bedrock variation  $\delta g_{bed}$ , **b** ice  $\delta g_{ice}$ , **c** water  $\delta g_{water}$ , and **d** the total topographic mass corrections  $\delta g_{TC}$ , estimated at the elevation 10 km above the reference surface

is used to obtain the vertically averaged density for the offshore regions (Fig. 5 in Mooney and Kaban (2010)). These data (as shown in Fig. 4a, b) are used to estimate the gravity effect of the sedimentary layer. The Moho depth model (Szwilius et al. 2019) is obtained globally with  $1^\circ \times 1^\circ$  spatial resolution using geostatistical analysis of the seismic investigations from the U.S. Geological Survey Global Seismic Catalog database. Due to the sparse coverage for oceans, we use the Moho depth provided by CRUST1.0 (Laske et al. 2013) in the oceanic region. In addition, the average crystalline crust P-wave velocities provided by Szwilius et al. (2019) are used to obtain the mean crustal density  $\bar{\rho}$ . The following empirical relations between the crustal P-wave velocity and density are applied (Szwilius et al. 2019),

$$\begin{aligned}\bar{\rho}[\text{kg/m}^3] &= 350 + 385v_p[\text{km/s}], \text{ for oceans} \\ \bar{\rho}[\text{kg/m}^3] &= 590 + 346v_p[\text{km/s}], \text{ for continents}\end{aligned}\quad (15)$$

where  $\bar{\rho}$  is the average crustal density and  $v_p$  is the average crustal P-wave velocity. The Moho depth resulting from the merging and the mean crustal densities used in the calculations are shown in Fig. 4c, d.

For the topographic mass corrections, the ice, water, and bedrock surfaces are taken from the CRUST1.0 model (Laske et al. 2013), which is derived by binning and averaging the ETOPO1 data in 1-degree cells (Amante and Eakins 2009). The average topographic density  $\rho_0 = 2670 \text{ kg/m}^3$  (Claessens and Hirt 2013; Grombein et al. 2016; Hirt et al. 2019; Rexer et al. 2016) is assumed for the bedrock. The densities of the ice and seawater layers are set to be 920 and 1020  $\text{kg/m}^3$ , respectively. To locate the topographic masses in space and take the ellipticity of the Earth's shape into account, the reference surface is defined by Grombein et al. (2016)

$$R_0 = r_E + N, \quad (16)$$

where  $r_E$  is the latitude-dependent radius of a reference ellipsoid (GRS80 is used in this study) with the semi-major axis  $a$  and the second numerical eccentricity  $e$ ,

$$r_E = \frac{a}{\sqrt{1 + e^2 \sin^2 \varphi}}. \quad (17)$$

$N$  denotes the geoid undulation, which is determined from the gravity model EGM2008 to degree and order 360 (Ince et al. 2019) in this study.

In order to compute the gravity effect of the entire lithosphere, each layer is decomposed into tesseroïd mass bodies with  $1^\circ \times 1^\circ$  arc-deg spatial resolution in the horizontal directions. The initial radial dimension and geocentric radius of each tesseroïd are determined by the layer's upper and lower boundary surfaces. The gravity attraction of each layer is calculated as the sum of all tesseroïd elementary volumes. All calculations are performed at an elevation of 10 km above the reference surface.

### 3.1 Gravity Effects of the Water, Ice, and Bedrock

Figure 5a-c shows the gravity effects of the bedrock, ice, and water calculated at the surface of 10 km above the reference surface ( $R_0$ ). The bedrock contribution  $\delta g_{\text{bed}}$  (Fig. 5a) ranges from  $-1088 \text{ mGal}$  to  $432 \text{ mGal}$ . Positive values are mainly associated with the masses above the reference surface in the continents, while the negative ones indicate the



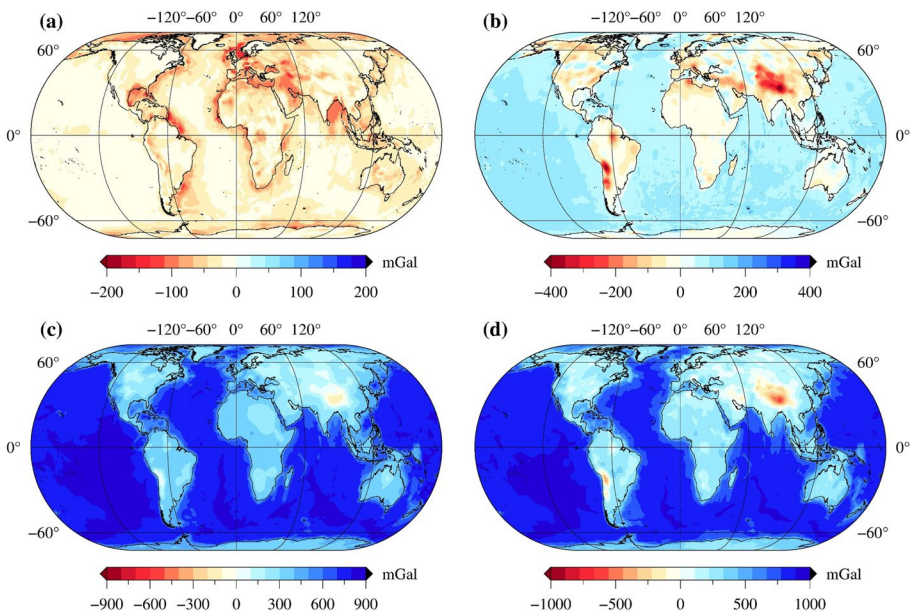
rock mass deficit in the oceans. The gravity effect of the ice  $\delta g_{ice}$  (Fig. 5b) is all positive with values ranging from 1 to 166 mGal and mainly limited to Greenland and Antarctica. Also, the water proportion  $\delta g_{water}$  provides a remarkable positive signal that ranges from about 80–420 mGal, which is mainly contributed by seawater.

Figure 5d depicts the total gravity effect of the topographic masses ( $\delta g_{TC}$ , Eq. 6). It ranges from –666 to 517 mGal, combining the positive effect of the mass excesses above the specified reference surface and the negative impact of mass deficits below this surface. Significantly high values are observed in the continental mountain ranges, such as the Tibetan Plateau and the Andes, while prominent low values are located over the marine areas, consistent with the findings of previous studies (Grombein et al. 2016; Tenzer et al. 2009).

### 3.2 Crustal Gravity Anomalies

To account for the gravity effect of the crustal layers, we first set up a reference density model with the parameters as presented in Table 1 (as described in Sect. 2.3). It corresponds to a continental crust with zero topography, a 15 km thick upper crust with a density of 2700 kg/m<sup>3</sup>, a 25 km thick lower crust with a density of 2940 kg/m<sup>3</sup>, and an uppermost mantle down to 75 km with a density of 3300 kg/m<sup>3</sup>, which is the similar reference density model employed in the regional studies by Kaban et al. (2016b) and Mooney and Kaban (2010).

Figure 6a–c shows the gravity fields created by the sedimentary layer, crystalline crust, and Moho relative to the reference model. As shown in Fig. 6a, the gravity effect of the low-density sedimentary layer ( $\delta g_{sed}$ ) is negative relative to the reference crust, and its



**Fig. 6** Gravity effects (as described in Sect. 2.3) of **a** the sedimentary layer  $\delta g_{sed}$ , **b** crystalline crust layer  $\delta g_{crust}$ , **c** Moho correction  $\delta g_{Moho}$ , and **d** the total gravity anomalies of the crust relative to the three-layer reference model ( $\delta g_{cs1}$ )

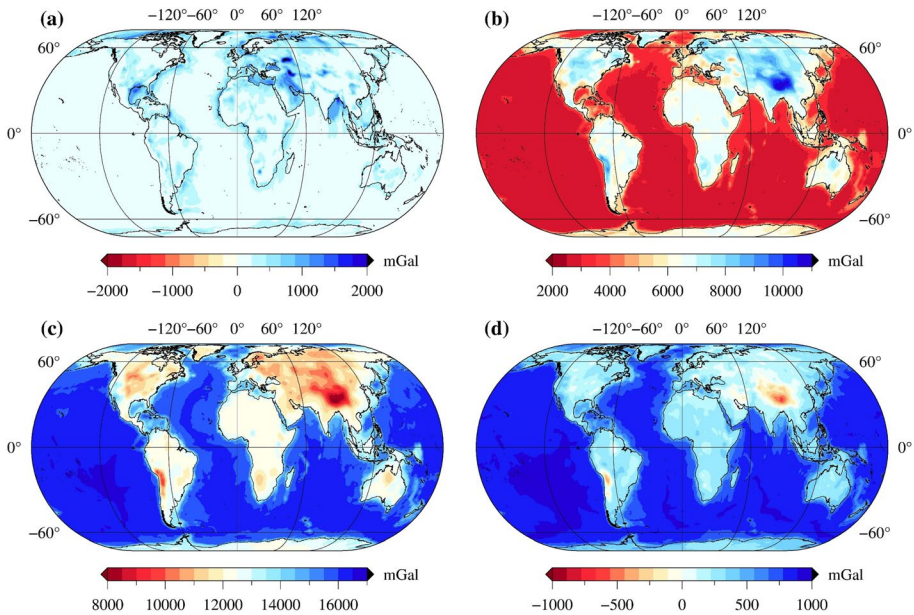


**Fig. 7** Gravity effects (as described in Sect. 2.4) of **a** the sediments  $g_{\text{sed}}$ , **b** crustal layers  $g_{\text{crust}}$ , **c** uppermost mantle above 75 km  $g_{\text{Moho}}$ , **d** the gravity anomalies ( $\delta g_{\text{cv}2}$ ) of the sediments, crust, and Moho variation after flattening the terrain at the surface relative to the three-layer homogenous model

extreme value reaches  $-169$  mGal in the 18 km thick depocenter of the Barbados Accretionary Prism. Large negative values coincide with deep sedimentary basins and the continental margins with major marine sediment accumulations. The gravity anomalies produced by the crystalline crust  $\delta g_{\text{crust}}$  (Fig. 6b) are even more significant, ranging from about  $-445$  to 216 mGal. Similarly, if the density of the modeled crust is lower relative to the reference crust, the gravity effect of this volume is negative, and vice versa. For the Moho correction (Fig. 6c), any uplift of the Moho interface relative to the average Moho depth in the reference crust (i.e.,  $D_2 = -40$  km in Table 1) produces a positive gravity signal since the mantle materials with relatively high density are replacing the reference lithosphere (Mooney and Kaban 2010). A typical thickness for the oceanic crust is 6 km, and for the continental crust is about 35 km thick (Turcotte and Schubert 2014). Therefore, the ocean region is dominated by extremely high values in the Moho correction, as shown in Fig. 6c. On the contrary, deepening the Moho boundary produces a negative signal, such as in the Tibetan Plateau and the Andes. Figure 6d shows the total crustal gravity effect generated by the sediment, crystalline crust, and Moho variation relative to the reference model. Due to the significant contribution of the Moho variations, the overall pattern of the crust correction is similar to the Moho correction, but its amplitude has a broader range between  $-620$  and 944 mGal.

Furthermore, we perform the forward modeling of the layer-based masses with their actual densities, as introduced in Sect. 2.4. The resultant maps are shown in Fig. 7. The gravity field of the sediments (Fig. 7a) varies from 73 to 2133 mGal. The most pronounced maximum values are located over the continental margins and sediment basins, which have the same pattern as that calculated with density contrast (Fig. 6a). The gravity map of the crustal layer (Fig. 7b) exhibits high values reaching up to  $\sim 10,775$  mGal in the continents due to

the thickened crust. Low values are observed in the ocean regions owing to the thin oceanic crust. The gravity field of the masses in the uppermost mantle below the Moho (Fig. 7c) also shows the same pattern as the results with density contrasts (Fig. 6c), but its amplitudes vary from 7925 to 16,681 mGal. Figure 7d shows the crustal gravity anomalies  $\delta g_{cs2}$  calculated by Eq. (13) with the actual densities, which are consistent with the results obtained by the approach using density contrasts ( $\delta g_{cs1}$ , Fig. 6d). The mean difference between these two anomalies is only about 0.05 mGal. This comparison demonstrates that the calculations using both strategies for considering the gravity effects of the crust are correct.

### 3.3 Mantle Gravity Disturbances

In this section, we apply the above corrections for the observed gravity field to obtain the residual mantle gravity disturbances. First, the free-air gravity disturbances (Fig. 8a) are

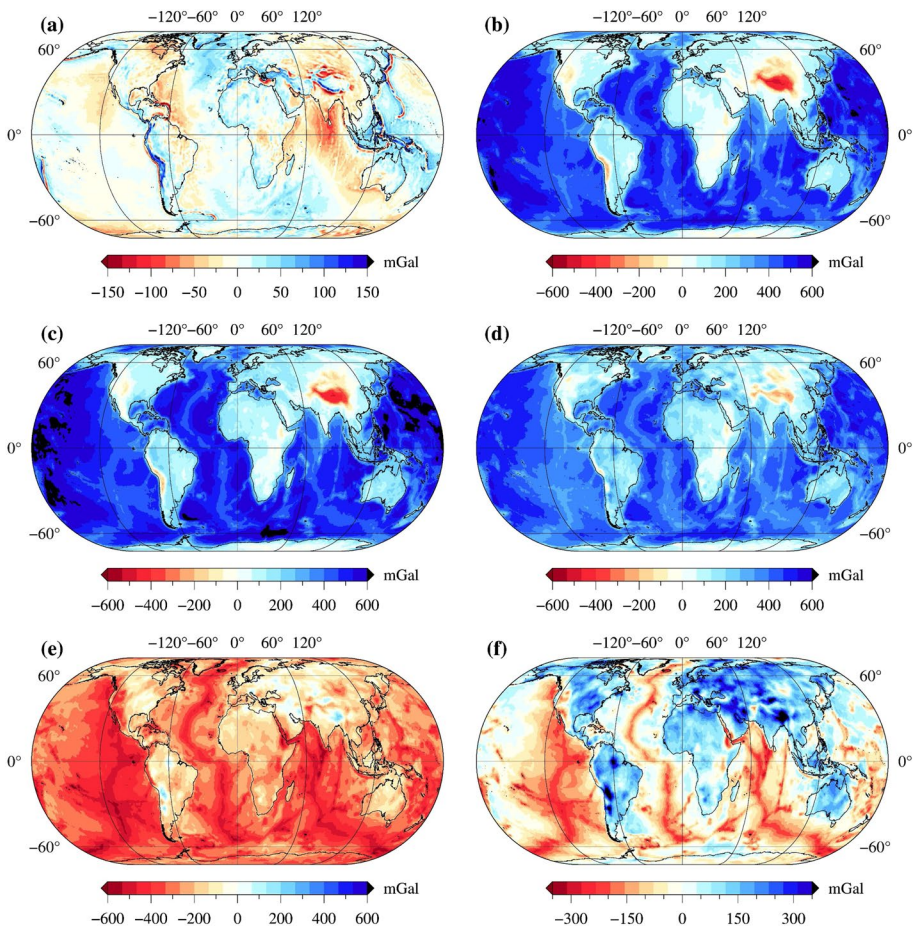


**Fig. 8** The gravity fields of the crust and mantle. **a** Free air gravity disturbances  $\Delta g_{FA}$ , **b** Bouguer gravity disturbances  $\Delta g_{BG}$ , **c** the sediment-stripped gravity disturbances  $\Delta g_{SS}$ , **d** the crust-stripped gravity disturbances  $\Delta g_{cs}$ , **e** mantle gravity disturbances  $\Delta g_m$  relative to the reference crust model, and **f** the mantle gravity disturbances with the removed mean value of  $-280.738$  mGal

calculated using the gravity field model EIGEN-6C4 (Ince et al. 2019) to degree and order 180. As shown in Fig. 8a, the amplitude variations in the free-air gravity disturbances are mostly as small as  $\pm 100$  mGal. The low amplitudes of the observed gravity field are the result of mass compensation in the interior of the whole Earth. The strong dipole-type anomalies correspond to large orogenic belts or subduction zones, such as the Himalayas, Andes, and the western Pacific subduction belt. The Bouguer gravity disturbances (Fig. 8b) are obtained by removing the gravity effect of the topographic masses ( $\delta g_{TC}$ , Fig. 5d) from the free air gravity disturbances. This gravity field ranges from about  $-499$  to  $648$  mGal, as presented in Table 3, and reflects the mass anomalies beneath the surface.

We increase the residual anomaly by removing the effect of low-density sediment ( $\delta g_{sed}$ , Fig. 6a) from the Bouguer gravity disturbances, and the resulting anomalies, as shown in Fig. 8c, correspond to the sediment-stripped gravity disturbances (Eq. (9)). Likewise, we remove the gravity effect of variations in the crustal thickness and densities down to Moho ( $\delta g_{crust}$ , Fig. 6b) for the crust-stripped gravity disturbances (Eq. 10) as shown in Fig. 8d. The corrections combining the sedimentary and crustal layers are equivalent to the Bouguer correction extended from the surface to the Moho (Kaban et al. 2016b; Mooney and Kaban 2010). The resulting crust-stripped gravity disturbances vary from  $-276$  to  $594$  mGal (Table 3). Since the contribution of density heterogeneities in the entire crust has been removed, this field mainly reflects the gravity signal from the Moho variation and underlying mantle density anomalies, and it is a suitable candidate for estimating the Moho variations (Kaban et al. 2022; Tenzer and Chen 2019).

After removing the Moho corrections from the crust-stripped gravity disturbances, we obtain the mantle gravity disturbances (Eq. 11) (Fig. 8e) ranging from  $-607$  to  $253$  mGal. Since the absolute value of the mantle gravity field depends on the choice of the reference crust model, we reduce the mean value of this field ( $-280.738$  mGal) as suggested by previous studies (Kaban et al. 2003, 2016b; Mooney and Kaban 2010; Shulgin and Artemieva 2019). The resulting mantle gravity disturbances are shown in Fig. 8f. The most striking feature is the significant positive anomalies ( $> 150$  mGal, reaching up to  $534$  mGal) associated with the continental interiors. These high anomalies are mainly distributed in central and southeastern North America, eastern and southern South America, western Africa, central Australia, and most of Eurasia. Pronounced negative anomalies are observed over the mid-oceanic ridges with values smaller than  $-150$  mGal. Negative anomalies are also found in western North America, the East-African Rift, and the Red River.

The significant positive anomalies generally agree with the findings of the earlier global study based on CRUST2.0 (Kaban et al. 2003). However, many significant differences also exist. For example, Kaban et al. (2003) presented broad positive anomalies in most

**Table 3** The statistics of the computed fields

Gravity fields	Minimum (mGal)	Maximum values (mGal)	Mean (mGal)	Standard deviation (mGal)
$\Delta g_{FA}$	$-271$	246	$-1$	29
$\Delta g_{BG}$	$-499$	648	284	200
$\Delta g_{cc}$	$-480$	673	323	200
$\Delta g_{cs}$	$-276$	594	284	154
$\Delta g_m$	$-607$	253	$-281$	117
Demeaned $\Delta g_m$	$-326$	534	0	117



ocean regions with thermally induced density variations correction. Such thermal correction is not considered in our study. This mantle gravity pattern is consistent with previous regional results in the North American continent (Kaban et al. 2014; Mooney and Kaban 2010). These studies presented strong negative mantle anomalies in western North America and the adjacent oceanic region and pronounced positive anomalies in the eastern portions of the continental interior, which agrees well with our results in the same area. This is because the initial crustal models employed from these calculations were all compiled from the same database, i.e., USGS global seismic catalog database (Mooney 2015). Furthermore, our results are consistent with the residual upper mantle gravity disturbance map in other regional studies based on regional crustal models (Kaban et al. 2016b; Shulgin and Artemieva 2019). For example, in the European-North Atlantic region, extremely low values are observed in Fig. 8f along the mid-Atlantic ridge, increasing from the mid-ridge to the European continents, while high values are widespread in East European Craton with significantly varying amplitudes. This pattern is in good agreement with a recent study in the same region (Shulgin and Artemieva 2019). For Asia, high positive values are observed in the old blocks or cratons, e.g., Siberian Craton, Tarim, and northern Indian Craton; in contrast, negative values correspond to active tectonic units or back-arc basins, e.g., Altay-Sayan orogen, Baikal rift system, and Sea of Japan, which are consistent with the findings by Kaban et al. (2016b).

It is essential to assess the uncertainties of the corrections for the mantle disturbance map. According to previous investigations, the potential errors in the thickness and density of the used crustal model are the major contributors to the overall error in the corrections of the mantle anomalies, which may be at the level from a few tens to more than one hundred mGal over the continents (Artemieva et al. 2019; Herceg et al. 2016; Kaban et al. 2003; Mooney and Kaban 2010; Tenzer et al. 2009). For comparison, we perform the same calculations based on the CRUST1.0 model, and the parameters and results are shown in the supplementary materials (Table S1, Figs. S1–S3). Overall, the large-scale anomalies based on CRUST1.0 (Figure S2f) are consistent with the results shown in Fig. 8f. At the same time, large differences (Fig. S3) are found in most of Eurasia and southern America, e.g., the Tibetan Plateau, the Tarim basin, Pamir, Altay-Sayan, Anatolia, Urals, and the Andes. Since the resulting mantle gravity disturbances are significantly larger (with extremes of approximately  $\pm 300$ ) than the possible uncertainty of the calculation, we suppose that the large-scale anomalies are reliable. Detailed estimations of this error are complex and need further analysis of the global crustal model, which is out of the scope of this study.

## 4 Mantle Gravity Disturbances and Implications

### 4.1 Comparison of the Mantle Gravity with Other Geophysical Data

In this section, to eliminate the uncertainty related to small-scale anomalies, we perform a spherical harmonic analysis of the global mantle gravity data, determining a finite number of coefficients by direct integration over the sphere (Pollack et al. 1993). The resulting mantle gravity disturbances are restricted to a spectral resolution of degree/order 36, corresponding to a spatial resolution of  $\sim 500$  km half-wavelengths. By this, we emphasize the globally significant well-determined large-scale mantle anomalies.

Figure 9a–d shows the resulting mantle gravity disturbances, the lithospheric thickness (Priestley et al. 2019), and the shear wave velocities at 150 km and 500 km depths

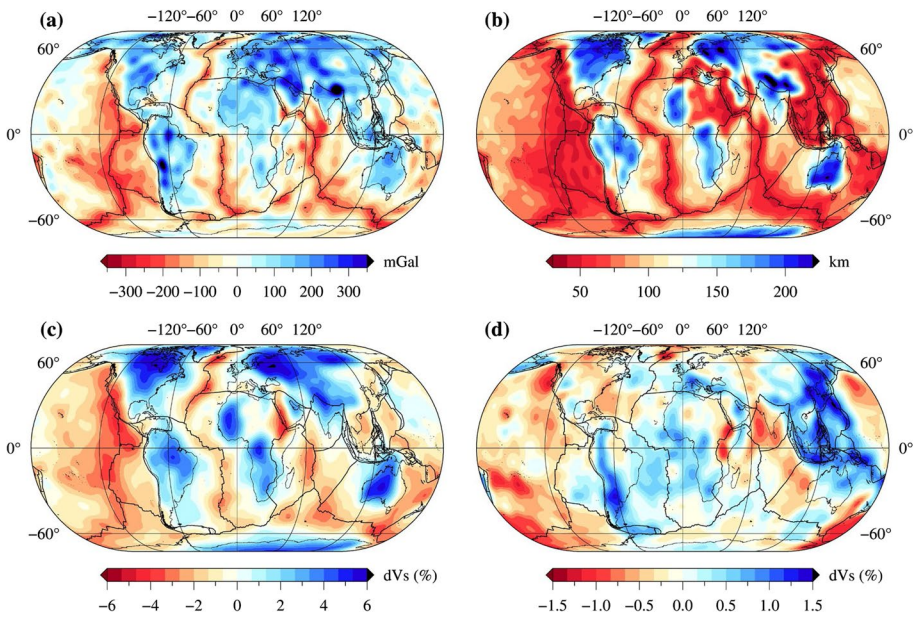


**Fig. 9** **a** Mantle gravity disturbances truncated up to degree 36. **b** Lithospheric thickness (Priestley et al. 2019). Global Vs velocities at **c** 150 km depth and **d** 500 km depth averaging over 20 datasets (Hosseini et al. 2018). The present-day plate boundaries (thick black lines) are derived from Matthews et al. (2016). All data are restricted to the degree/order 36 spectral resolution

averaging over 20 available global seismic datasets (Hosseini et al. 2018). The global lithospheric thickness model (Fig. 9b) is obtained from CAM2016 (Priestley et al. 2019), which was derived from multimode surface-wave tomography and petrology. Thick lithosphere of 150–250 km is found beneath most cratonic regions, such as the Canadian, West African, Congo, Siberian, Antarctic, Australian, and Indian cratons. Thin lithosphere (less than 50 km) is observed in the mid-oceanic ridges and many regions near ongoing or recent subduction or orogenies, such as western North and South America, western Europe, and eastern Asia (Steinberger and Becker 2018). The mantle gravity disturbances (Fig. 9a) and the lithospheric thickness map (Fig. 9b) have a similar pattern in most of these regions, except for some areas, e.g., east Asia and the Mediterranean. The thick lithosphere in cratonic regions is associated with high positive mantle gravity anomalies (up to 350 mGal). In contrast, the thin lithosphere is consistent with low mantle gravity values. Notably, the thinnest lithosphere in the mid-oceanic ridges (50 km and less) corresponds to extremely low mantle gravity anomalies ( $\leq -150$  mGal).

Figure 10a displays the statistical relationship between the lithospheric thickness and the mantle gravity disturbances between the latitudes  $-75^\circ$  and  $75^\circ$  ( $150 \times 150$  km cells). The regions with relatively thin lithosphere have positive and negative mantle gravity values, but the areas with negative anomalies predominate. Another feature is that the gravity anomalies increase with the lithosphere thickness (see the dashed line in Fig. 10a). The increasing trend of the mantle gravity anomalies with the lithosphere thickness demonstrates that the thickness and density variation of the lithosphere

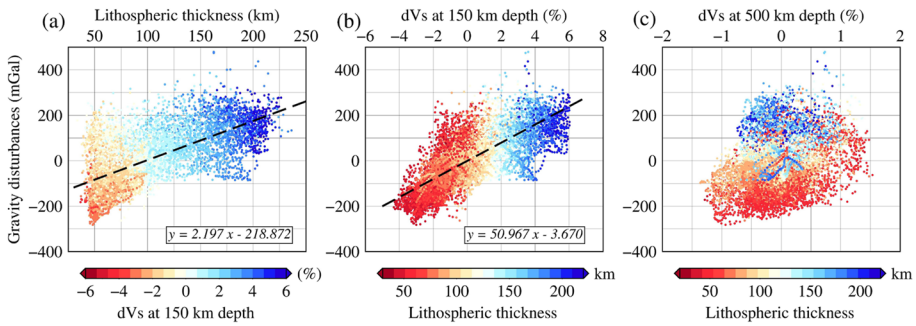


**Fig. 10** The relationship between the mantle gravity disturbances and **a** the lithospheric thickness, the Vs velocities at **b** 150 km depth, and **c** 500 km depth. The black dashed lines in Fig. 9a and b are derived from linear data regression with a grid of  $150 \times 150 \text{ km}^2$

mantle is one of the dominant contributors to mantle gravity anomalies. Without density contrast between the lithospheric root and the surrounding mantle, the lithospheric thickness variation could not impact the mantle gravity field. Remarkably, the mantle gravity disturbances in the regions with thick lithosphere (larger than  $\sim 200 \text{ km}$ ) are nearly all positive, mainly corresponding to old cratons.

Figure 9c, d shows that slow velocities at 150 km depth are mainly associated with mid-ocean ridges, and significant fast velocities are found beneath the continental cratons and old oceanic lithosphere. Comparing the velocity map at 150 km depth (Fig. 9c) and the mantle gravity map (Fig. 9a), we observe that the velocities agree with the trend of the mantle gravity disturbances. Similarly, the statistical chart (Fig. 10b) displays a highly positive linear correlation between these data, consistent with the relationship between velocity and density summarized by rock physics studies (Christensen and Mooney 1995). In contrast, no apparent linear relationship is observed (Fig. 10c) between the mantle gravity and the Vs velocities at 500 km depth. The consistent patterns of the mantle gravity disturbances, lithospheric thickness, and seismic wave velocities at 150 km depth indicate that the density variations generating the mantle gravity field are most likely located in the upper mantle.

Temperature and compositional variations are the most critical factors contributing to the mantle gravity field (Kaban et al. 2014; Mooney and Kaban 2010; Shulgin and Artemieva 2019; Tesauro et al. 2014b). As we know, shear wave velocities are dominantly controlled by temperature variations (Goes 2002; Tesauro et al. 2020). In the cratonic regions, the remarkable fast velocities at 150 km depth mainly reflect the relatively cold thermal state of the cratonic roots. The low temperatures could increase the density, resulting in significant positive mantle gravity anomalies associated with the cratons. On the other hand, the chemical depletion in Al, Ca, and Fe makes the lithospheric roots buoyant and highly viscous (Pearson and Wittig 2014; Pearson et al. 2021). Based on mantle xenoliths and the negligible free-air gravity and geoid anomalies, previous studies proposed the isopycnic hypothesis in the old continental nuclei (Jordan 1978). This hypothesis states that excess density of thermal origin is nearly canceled by density deficit due to compositional depletion within the mantle lithosphere (Jordan 1978).

In contrast to the isopycnic hypothesis, the new mantle gravity disturbances in this study (Fig. 9a) suggest density excess in the continental roots relative to oceans. Although the composition-induced density reduction may partly compensate for the excess density of

thermal origin, the gravity effect as a result of these two effects is still primarily positive in most continents. Specifically, the strong positive anomalies corresponding to cratons suggest that their lithospheric roots are much denser than the ambient mantle. The denser sub-cratonic lithospheric mantle (with respect to isopycnic) is also supported by recent residual topography, gravity, and geodynamic studies (Mooney and Vidale 2003; Wang et al. 2023; Wang et al. 2022a, b).

On the one hand, the dense lithospheric roots may reflect the effect of the temperature being dominated over the composition, as indicated by the high seismic velocities associated with the cratonic lithosphere (Fig. 9c). The cratonic mantle is, on average, 500–700 °C cooler than the ambient mantle (~1400 °C) (Lee et al. 2011). According to  $\Delta\rho = -\alpha\Delta T\rho_0$ , and  $\alpha = 3.47\text{--}4.91 \times 10^{-5} \text{ K}^{-1}$  at different pressure in the upper mantle (Schutt and Leshner 2006), this average temperature difference results in a density increase of about 58–113 kg/m<sup>3</sup> due to thermal contraction (i.e., 1.75–3.43% decrease in density), assuming an average density of 3300 kg/m<sup>3</sup> in the upper mantle. Schutt and Leshner (2006) pointed out that 1% melt depletion is equivalent in density effect to a 3–15 °C increase in temperature (depending on pressure). Their model predicted that the density effect of melt depletion is too small to produce an isopycnic mantle at shallower depths above ~110 km. On the other hand, the tectonic processes, like refertilization and metasomatism, could also result in denser roots at greater depths with mafic compositions enrichment (e.g., garnet-lherzolite or eclogite) in the cratonic settings, which are supported by xenolith data (Cherepanova and Artemieva 2015; Griffin et al. 2003; Lee et al. 2011; Wang et al. 2023).

To confirm the effect of the denser cratonic roots on the mantle gravity field, we estimate the gravity effect of 40 kg/m<sup>3</sup> density surplus in the cratonic roots based on the LITHO1.0 model (Pasyanos et al. 2014). The calculation surface is 10 km height above the geoid. The lithospheric mass deeper than 110 km (i.e., the 110 km depth to the lithospheric bottom) is considered in the forward calculation. Figure S4 (in the supplementary material) shows that considerable positive gravity anomalies (up to 310 mGal) are concentrated in the craton regions due to their extremely thick roots (>110 km) and the assumed density surplus (40 kg/m<sup>3</sup>).

But how do cratons achieve an isostatic compensation in the presence of a denser root? Previous studies indicate that the Moho under cratons is, on average, deeper than other continental areas (Kaban et al. 2003; Mooney et al. 1998). A recent study (Wang et al. 2023) shows a nearly linear dependence of crustal thickness on the lithosphere–asthenosphere boundary (LAB) depth for almost all cratons. Consequently, we infer that these dense cratonic roots are compensated by the thickness and density variations of the crust as well as by their chemical depletion (Hyndman and Lewis 1999; Kaban et al. 2003, 2014; Mooney and Vidale 2003; Tesauro et al. 2014b; Wang et al. 2022b), which could explain the close to zero free-air and geoid anomalies over cratons.

For the oceanic regions, we find particularly low values of the gravity, lithospheric thickness, and  $V_s$  velocities at 150 km depth (Fig. 9) associated with the mid-ocean ridges, which is in agreement with previous studies (Kaban et al. 2003; Tenzer and Chen 2019; Tenzer et al. 2015). All values gradually increase toward the oceanic basins. The global heat flow measurements (Davies 2013) show high heat flow above young oceanic crust and low heat flow in continental shields and cratons. Furlong and Chapman (2013) pointed out that the continental heat flow primarily arises from radiogenic heat production in the crust, while oceanic heat flow is dominated by lithospheric cooling while the plate moves away from the mid-ocean ridges. Thus, the increase in density and thickness due to conductive cooling of the oceanic lithosphere could partly explain the gravity-increasing pattern from the mid-ocean ridges to the oceanic basins.



On the other hand, Fig. 9b shows that the lithosphere near the mid-ocean ridges is much thinner than 100 km. Therefore, the low velocities at 150 km depth chiefly indicate high temperatures of the oceanic upper mantle relative to the cold lithosphere of the continents (Faul and Jackson 2005). As a result, the remarkable low mantle gravity disturbances associated with the mid-ocean ridges also stem from the temperature-induced density decrease in the asthenosphere. This low-density asthenosphere promotes buoyant mantle upwellings beneath the mid-ocean regions, as supported by geodynamic and geophysical studies (Behn et al. 2007; Eakin et al. 2018; Morgan and Forsyth 1988).

Notable inconsistencies between gravity, lithospheric thickness, and  $V_s$  velocity at 150 km depth are found in some regions, such as east/southeast Asia and the Mediterranean. These regions are located near active or extinct subduction zones, and they are characterized by thin lithosphere and low  $V_s$  velocity at 150 km depth, but with relatively high mantle gravity disturbances. Compared with the  $V_s$  velocities at 500 km depth in the transition zone (Fig. 9d), we attribute the high mantle gravity in these regions to deeper density variations caused by dense subducted lithospheric plates as indicated by the study of gravity gradients (Panet et al. 2014).

## 4.2 The Mantle Gravity Disturbances in the Continents of the Northern Hemisphere

Although the large-scale features of the residual mantle anomalies are similar to previous global calculations (Kaban et al. 2003; Tenzer and Chen 2019), e.g., the generally positive anomalies over the old continental parts and negative anomalies over the mid-oceanic ridges, we further find many regional differences, which result from the improved crustal model used in this study. Since the seismic determinations of the Moho depth are very irregular, we concentrate on the regions well covered by seismic observations, such as North America and a significant part of Eurasia.

Figure 11 shows the mantle gravity disturbances over the North American Continent. The most striking feature is the high anomalies associated with the central and eastern regions and the low values distributed in the western margin and the eastern Pacific Ocean. The mantle gravity disturbances reflect the density heterogeneity in the mantle, mainly resulting from the thermal and compositional variation in the uppermost mantle (Kaban et al. 2014; Tesauro et al. 2014b).

As shown in Fig. 11, the mantle gravity amplitudes are highly variable in the cold provinces in the central and eastern North American continent. The most pronounced positive mantle anomalies (150–350 mGal) are found in the Slave/Rae/Hearne Province, Hudson Bay Basin, and Yavapai-Mazatzal Province. Seismic studies show significant high-velocity anomalies in the upper mantle beneath these regions, indicating cold and thick lithospheric roots (Pearson et al. 2021; Schaeffer and Lebedev 2014). Therefore, we attribute these strong positive mantle disturbances in these provinces to the significant density increase due to the cold thermal state of the thick lithospheric roots. Particularly, mantle gravity anomalies with relatively low magnitudes of  $-50$ – $100$  mGal correspond to the oldest Superior Craton and northern Rae Craton. We infer that the reduced mantle anomalies associated with these old cratons may result from their highly depleted roots compared with other weakly depleted cratons, as evidenced by Kaban et al. (2014) and Tesauro et al. (2014b). This could partly balance the density increase due to the cold temperature, and ultimately, decrease the mantle gravity anomalies. In addition, part of the positive mantle anomalies, such as in the Grenville-Appalachian orogeny, may stem from dense remnant slab fragments in the uppermost mantle (Kaban et al. 2015; Mooney and Kaban 2010).

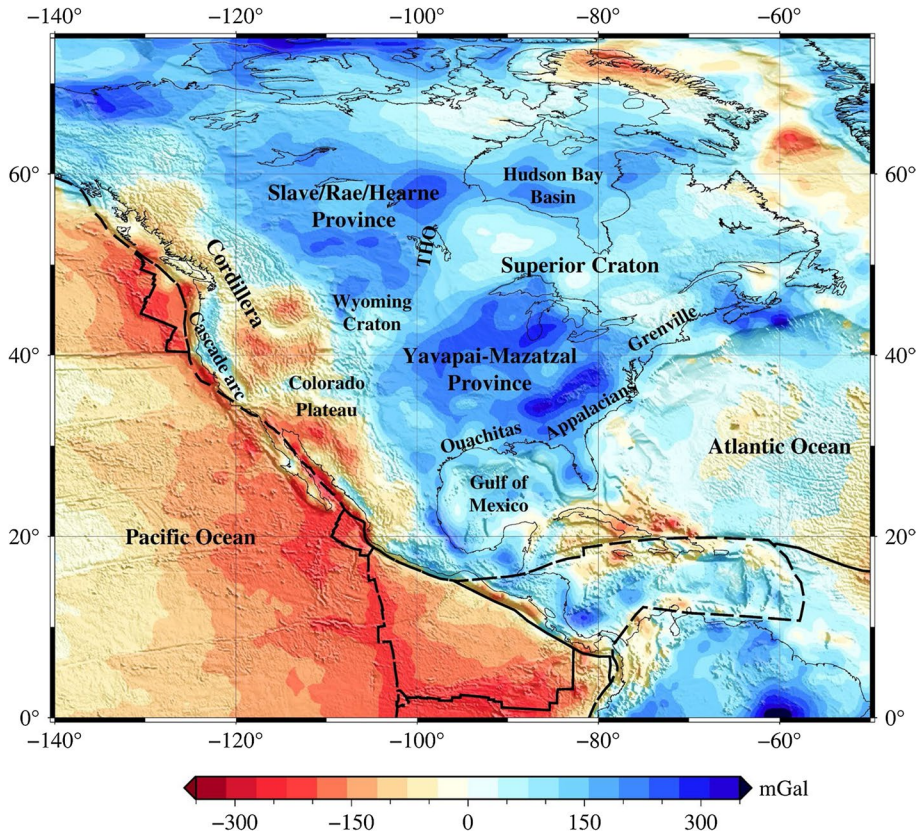


**Fig. 11** Mantle gravity disturbances and main tectonic features of the North American Continent. The tectonic features are modified according to Clouzet et al. (2018). THO is an abbreviation that stands for Trans Hudson Orogen. The thick black lines represent the plate boundaries derived from Matthews et al. (2016)

In western North America, significant negative mantle anomalies mixed with small positive anomalies are observed in Fig. 11. These negative anomalies are primarily distributed along the Cordillera Province and surprisingly connect with the pronounced negative anomalies in the mid-ocean ridge of the Pacific Ocean. These negative mantle gravity anomalies suggest the presence of mass deficits within the mantle, which may be associated with the thermal expansion of the buoyant hot mantle (Becker et al. 2014, 2015; Hyndman and Currie 2011; Hyndman and Lewis 1999; Parsons et al. 1994). Furthermore, low  $P_n$  values are also observed in the western margin (Buehler and Shearer 2017; Tesouro et al. 2014a), supporting the thermal origin. Compared with the extremely low anomalies along the plate boundaries, the gravity amplitudes in the western margins are significantly smaller, reflecting the balance between the warmer temperature and composition in the upper mantle. In addition, small positive anomalies are observed in the Cascade arc, which may be a signal of the subducting lithosphere (Kaban et al. 2014).

Figure 12 displays the mantle gravity disturbances of the European Continent. Compared with earlier global studies (Kaban et al. 2003; Tenzer and Chen 2019; Tenzer et al. 2015, 2009), our results show better correspondence between the mantle anomalies and the geological features. A large-scale strong positive anomaly (200–400 mGal) coincides

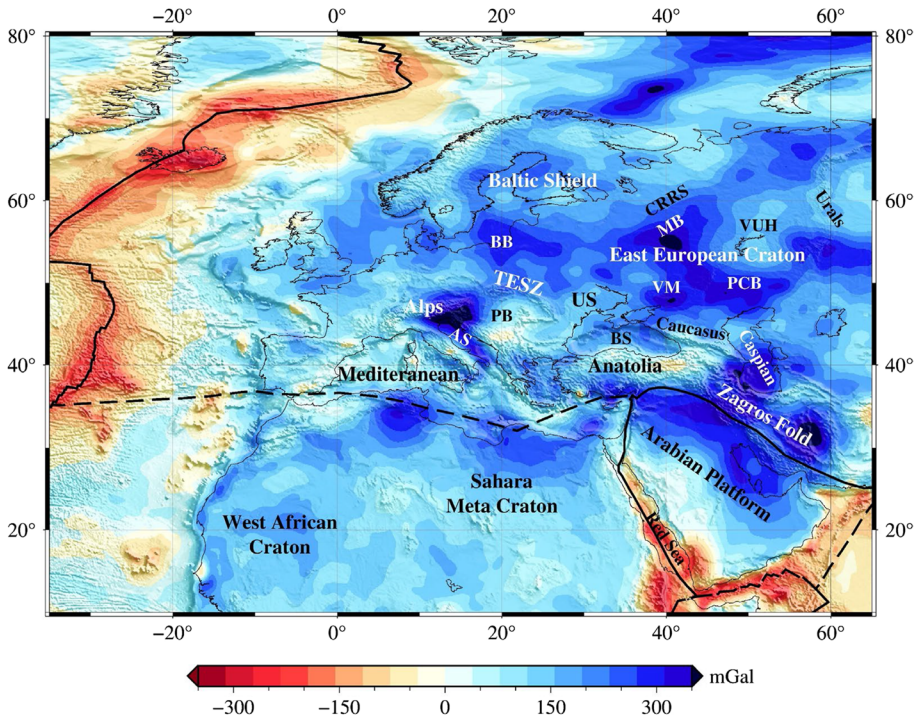


**Fig. 12** Mantle gravity disturbances and main tectonic features of the European Continent. Abbreviations: AS, Adriatic Sea; BB, Baltic Basin; BS, Black Sea; CRRS, Central Russia Rift system; MB, Moscow Basin; PB, Pannonian Basin; PCB, Peri-Caspian Basin; TESZ, Trans European Suture Zone; US, Ukrainian Shield; VM, Voronezh Massif; VUH, Volga-Uralian High. Symbols are the same as in Fig. 11

well with the East European Craton (EEC) and Baltic Shield. Seismic studies (Chang et al. 2010; Schaeffer and Lebedev 2013; Schivardi and Morelli 2011; Zhu et al. 2015) revealed high velocities down to depths more than 250 km beneath this region, representing a cold and old lithospheric lid. The long-wavelength positive mantle disturbances corresponding to the EEC are likely related to the presence of a thick cold lithosphere. Laterally, the mantle gravity values vary significantly within the EEC, reflecting strong density heterogeneities in the lithospheric mantle. Geological studies recognized three large sub-cratons separated by several rift systems within the EEC, including Baltica, Sarmatia consisting of the Ukrainian Shield (US) and the Voronezh Massif (VM), and the Volga-Uralia High (VUH) (Artemieva and Thybo 2013). Relatively low values ( $< 150$  mGal) are found in the northeastern Baltic Shield, Volga-Uralian High, and southern Ukrainian Shield, which possibly reflect the most depleted composition of the Archean cratons (Jordan 1978; Shulgin and Artemieva 2019). High gravity values ( $> 300$  mGal) are observed in the Peri-Caspian Basin (PCB), Voronezh Massif, Moscow Basin (MB), and Baltic Basin (BB). In addition to the cold thermal origin, the high mantle gravity disturbances may also indicate chemical densification through metamorphic reactions of the lithospheric mantle (e.g., eclogitization) or mantle metasomatism in the cratonic settings (Barth et al. 2002; Shirey et al. 2001; Shulgin and Artemieva 2019).

The mantle gravity disturbances in Western Europe ( $-100$ – $100$  mGal) are significantly lower than in East Europe. As the major geologic and tectonic boundary between the EEC and Western Europe (Artemieva and Thybo 2013; Zielhuis and Nolet 1994), the Trans-European Suture Zone (TESZ) marks a significant mantle gravity gradient, indicating the density heterogeneities between the Precambrian craton and Phanerozoic accretion in Europe. It shows the presence of relatively low-density masses within the upper mantle in Western Europe, consistent with a high mantle temperature (Artemieva 2006, 2019). Eastward, the southern boundary of the high mantle gravity anomalies coincides with the Black Sea (BS), Caucasus, and northern Caspian, clearly depicting the south edge of the stable EEC (Gee and Stephenson 2006).

In the south of the European Continent, the tectonic domains in the Mediterranean region are characterized by small-scale E–W trending mantle gravity anomalies with positive or negative amplitudes (Fig. 12). The mantle structure in this region is complex due to the convergence of the Eurasian and African-Arabian plates (Jolivet and Faccenna 2000; Zhu et al. 2015). The small-scale positive or negative anomalies reveal the complicated mantle density heterogeneities in the Mediterranean, which may be related to the variations in lithospheric thickness, subducting/rollback slabs, and/or hot mantle upwelling. Notably, localized high values are found in the eastern Alps, Adriatic Sea (AS), and southern Anatolia, suggesting the presence of denser materials in the mantle. These high anomalies may be induced by the subducting slabs, which have been imagined as fast wave speed anomalies by seismic tomographic studies (El-Sharkawy et al. 2020; Van der Meer et al. 2018; Zhu et al. 2015). In contrast, low mantle gravity values distributed in the northern Anatolia, the Pannonian Basin (PB), and the western Mediterranean Sea indicate relatively light mantle materials, likely resulting from localized hot mantle upwellings within the upper mantle (Faccenna and Becker 2010, 2020; Faccenna et al. 2014; Hoernle et al. 1995).

In the Middle East (Fig. 12), prominent positive mantle gravity disturbances characterize the stable Arabian Platform, which can be explained by the high-density mantle at shallow depths, as Kaban et al. (2016a) suggested. High gravity anomalies are also observed in the Zagros fold belt, likely associated with a northward dipping high-velocity anomaly in the upper mantle (Agard et al. 2011; Van der Meer et al. 2018). On the other hand, significant negative anomalies reaching  $\sim -300$  mGal are localized along the Red Sea and the Gulf of Aden, likely related to the hot mantle of the Afar plume (Bonatti 1985; Chang et al. 2011; Faccenna et al. 2013). In northern Africa, strong positive anomalies are mainly distributed in the Sahara Meta Craton and West African Craton. However, since the Moho data are very scarce in this area, we do not analyze these anomalies.

Figure 13 shows the mantle gravity disturbances and tectonic features in Asia. We observe a large-scale strong positive anomaly ( $100$ – $300$  mGal) in the Siberian Craton, which consists of the Archean and early Proterozoic crust (Cherepanova et al. 2013; Pearson et al. 2021). This continuous gravity anomaly depicts the southern and eastern boundary of the stable craton along the Altay-Sayans orogen, Baikal Rift Zone in the south, and Verkhoyansk Ridge in the east and mainly reflects the density increase due to the cold and thick lithosphere. Additionally, the lateral variations in gravity values within the craton illustrate a heterogeneous root in thickness, composition, and temperature. As an example, the sub-longitudinal high-anomaly belt in the central part of the Siberian Craton corresponds to an extremely thick lithosphere ( $300$ – $350$  km) and low heat flow values ( $18$ – $25$  mW/m<sup>2</sup>) (Artemieva 2006; Cherepanova and Artemieva 2015). The gravity study of Cherepanova and Artemieva (2015) also pointed out that the significant lateral mantle gravity variations may be related to the depletion/fertilization of the lithospheric mantle beneath the craton.



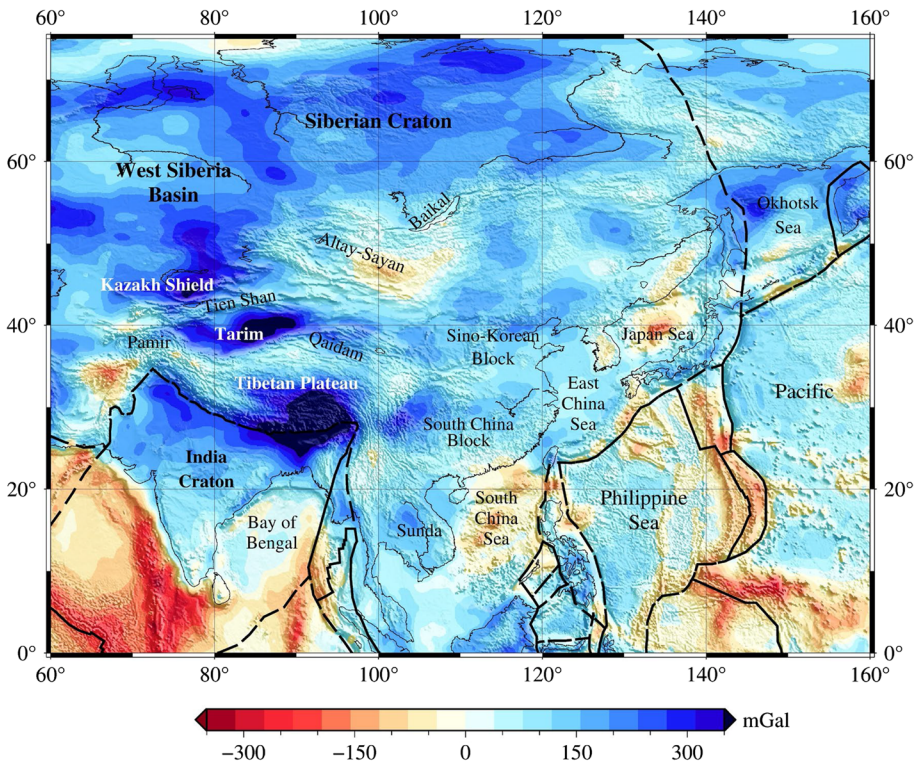


**Fig. 13** The mantle gravity disturbances and tectonic features of the Asia continent. Symbols are the same as in Fig. 11

To the west of the Siberian Craton, high positive anomalies (200–350 mGal) are also distributed in the northern, eastern, and southern parts of the West Siberia Basin, correlated with the Baikalian and Caledonian orogenies (Cherepanova et al. 2013). This gravity anomaly indicates the presence of high-density anomalies in the upper mantle below the basin, which may be caused by eclogitization (Cherepanova and Artemieva 2013). Furthermore, relatively low positive values (0–100 mGal) are observed at the central part of the basin, coinciding with the Phanerozoic Ob rift system. Global seismic tomography and thermal modeling indicate that the lithosphere of the West Siberia Basin is substantially thinner and warmer than the Siberian Craton (Artemieva 2006; Artemieva and Mooney 2001; Schaeffer and Lebedev 2013). The low positive gravity disturbances in the basin's center are likely caused by the emplacement of a hot, buoyant mantle beneath the thin lithosphere (Holt et al. 2012; Petrov et al. 2016; Saunders et al. 2005).

The active tectonic units, such as Pamir, Tien Shan, Altay-Sayan mountains, and the Baikal rift system, are characterized by relatively weak positive or negative mantle gravity disturbances (–150–100 mGal). Seismic studies (Lei 2011; Lei and Zhao 2007; Roecker et al. 1993) reported apparent low-velocity anomalies beneath Tien Shan, suggesting the upwelling of the hot materials from the mantle. Beneath the Altay-Sayan mountains, low-V anomalies have been imaged in the upper mantle, extending downward to at least 200 km depth (Huang and Zhao 2022; Koulakov and Bushenkova 2010). In the Baikal rift, the lithosphere is only 60–70

km (Lebedev et al. 2006), and a low- $V$  zone is also constrained in the uppermost 100 km depth (Huang and Zhao 2022; Koulakov and Bushenkova 2010). According to these observations, we infer that the negative gravity values stem from the thin lithosphere and buoyant mantle upflows beneath these regions (Kaban et al. 2016b; Lebedev et al. 2006).

As shown in Fig. 13, prominent strong positive anomalies ( $> 250$  mGal) are also found in the Kazakh Shield, northern Indian Craton, and Tarim basin. These regions are reported to be old stable blocks with a relatively thick lithosphere and prominent high- $V$  anomalies (Lei and Zhao 2007; Schaeffer and Lebedev 2013). Surprisingly, remarkably high values ( $> 250$  mGal) are also observed in the southern Tibetan Plateau, which connects with the high anomalies in the Indian Craton. The lithospheric thickness in this region is still controversial (Steinberger and Becker 2018). For the global models, LITHO1.0 (Pasyanos et al. 2014) shows a lithosphere of fewer than 150 km in the Tibetan/Himalayan region. In contrast, some tomography-based models show a thicker lithosphere (Priestley and McKenzie 2006; Priestley et al. 2019). The high mantle gravity values support a thicker lithosphere there. Besides, we suggest that the extremely high gravity anomalies also reflect the subducting/detached cold Indian slabs in the upper mantle beneath southern Tibet (Chen et al. 2017; Kind and Yuan 2010; Li et al. 2008; Zhao et al. 2011). On the contrary, the mantle gravity disturbances are relatively low ( $-50$ – $50$  mGal) in most other parts of the Tibetan Plateau, indicating anomalously hot upper mantle and thin/intermediate lithosphere, as suggested by seismic studies (Xia et al., 2023; Zhao et al. 2011).

Eastern Asia is one of the most active tectonic regions on Earth. Most of the area is characterized by low positive anomalies (50–100 mGal). Small-scale moderate positive anomalies (150–200 mGal) are associated with several old blocks, such as the Ordos basin in the Sino-Korean Block and the Sichuan basin in the South China Block. These high mantle gravity values indicate the presence of high-density anomalies in the upper mantle, consistent with the observations of relatively low surface heat flow and thick lithosphere beneath these blocks (An and Shi 2006; Sun et al. 2013; Wang 2001). Negative mantle gravity anomalies correspond to some back-arc basins, such as the South China Sea and the Japan Sea, as well as the subduction zones of the Philippine and Pacific plates. The negative values indicate low-density materials in the upper mantle due to hot mantle upwelling (Li et al. 2021; Tao et al. 2018). In summary, the significant lateral variation in the mantle gravity anomalies indicates that the mantle structure of this region is highly heterogeneous. Several geodynamic factors may contribute to the variations of the observed mantle gravity disturbances, including the lithospheric thickness variation (Steinberger and Becker 2018), hot mantle upwelling (Li et al. 2021), the subducting slabs (Panet et al. 2014; Tao et al. 2018), etc. The mantle gravity disturbances reveal the comprehensive effects of all the above density heterogeneities within the mantle.

## 5 Conclusions

Two different strategies have been proposed for the forward calculation of the gravity anomalies generated by density heterogeneities in the layered crust in the spatial domain. These are: (1) density contrast given by a reference lithosphere and (2) actual density variations. The gravity effects of each crustal layer, including the topography, the sediments, the crystalline crust, and the Moho variations, were calculated relative to a reference model using a subdivision of the masses with tesseroids. We applied these two strategies to evaluate the mantle gravity disturbance based on new sedimentary and Moho depth models on a global scale. Our results demonstrate that the two strategies yield the same patterns for the

gravity anomalies of the crust, confirming the correctness of both methods. The proposed methods are applicable to the forward calculation of the gravity anomalies for the layer-based crust models at both global and regional levels.

The large-scale patterns of the mantle gravity field are consistent with previous studies. The resulting mantle gravity map shows the largest positive anomalies (up to 350 mGal) associated with the continental interiors, mainly distributed in central and southeastern North America, eastern and southern South America, western Africa, central Australia, and most of Eurasia. The most pronounced negative anomalies are observed over the mid-oceanic ridges with values smaller than  $-200$  mGal. Negative anomalies are also found in western North America, the East-African Rift, and the Red River. Compared with the global lithospheric thickness and  $V_s$  velocities at 150 km depth, we observed an increasing trend of the mantle gravity anomalies with the lithosphere thickness and the  $V_s$  velocities. The consistent patterns between these three variables indicate that the resulting mantle gravity disturbances mainly reflect the density changes of the cratonic roots and underlying upper mantle, likely related to its thermal state non-completely compensated by the density decrease due to depletion.

Particularly, significant-high positive mantle gravity disturbances, thick lithosphere, and high  $V_s$  velocities at 150 km depth are found in most cratons, where the high velocities likely resulted from the reduced temperature of the thick cratonic roots. Although in these regions, the composition-induced density reduction caused by the chemical depletion could partly compensate for the excess density of thermal origin, the high residual mantle gravity anomalies indicate that the thermal effect still dominates over the compositional one associated with most of the cratons, suggesting denser roots. The tectonic processes, like re-fertilization and metasomatism, may also contribute to these denser roots at greater depths. In contrast, notable inconsistencies between the gravity and  $V_s$  velocities at 150 km depth are found in the regions close to the subduction zones (i.e., east Asia), characterized by low  $V_s$  velocity, but relatively high mantle gravity disturbances. We attributed the high mantle gravity in these regions to the deep density variations caused by remnants of the subducted slabs.

At regional scales, the new mantle gravity map shows good correspondence between the anomalies and geological features due to the improved crustal model. In North America, for example, different mantle disturbance patterns are observed over the Superior Craton and over the Slave/Rae/Hearne and Yavapai-Mazatzal Provinces, reflecting the density heterogeneity in the cratonic roots. Particularly, the reduced mantle anomalies associated with the oldest Superior Craton and northern Rae Craton may result from their highly depleted roots compared with other weakly depleted cratons. On the other hand, the negative anomalies distributed along the Cordilleran Province are connected with the pronounced negative anomalies in the mid-ocean ridge of the Pacific Ocean. These negative anomalies suggest the presence of mass deficits within the upper mantle, which may be associated with the thermal expansion of the buoyant hot mantle beneath the western margin of North America.

In Eurasia, large-scale strong positive anomalies coincide well with the Baltic Shield, East European Craton, and Siberia Craton, supporting thick, cold lithospheric lids in these regions. Laterally, the mantle gravity values vary significantly within these cratons, reflecting the lithospheric thickness variation as well as strong density heterogeneities because of the balance between composition and temperature. Some cratonic modifications, such as chemical densification through metamorphic reactions of the lithospheric mantle (e.g., eclogitization) or mantle metasomatism, may contribute to the highly variable mantle gravity disturbances within the cratons. In addition, a large number of the pronounced

small-scale positive mantle anomalies correspond well with old tectonic units, such as the Arabian Platform, Kazakh Shield, Indian Craton, Tarim, Ordos, and Sichuan basins. These high mantle gravity values indicate the presence of high-density anomalies in the upper mantle, supporting a cold and thick lithosphere beneath these stable blocks.

In active tectonic units, the mantle gravity disturbances are characterized by small-scale mantle gravity anomalies with positive or negative amplitudes, indicating a complicated mantle structure. For example, localized high or low values are found in the Mediterranean, which may be related to the variations in lithospheric thickness, subducting/rollback slabs, and/or hot mantle upwelling associated with the convergence of the Eurasian and African-Arabian plates. Small-scale high gravity anomalies observed in the Zagros fold belt and southern Tibet can be explained by the cold subducting/detached Arabian and Indian plates. Significant negative anomalies localized along the Red Sea and the Gulf of Aden spatially correlate with the Afar plume. The low negative mantle gravity disturbances in the Pamir, Altay-Sayan mountains, and the Baikal rift system are also correlated with low-velocity anomalies in the upper mantle, supporting the hot and thin lithosphere beneath these active regions. In addition, the negative mantle gravity anomalies also correspond to some back-arc basins, such as the South China Sea and Japan Sea, as well as the subduction zones of the Philippine and Pacific plates, which indicate low-density materials in the upper mantle due to hot mantle upwelling. Consequently, our improved results provide important implications for the mantle structure and dynamics on regional and global scales.

Note that the resulting mantle gravity disturbances are influenced by both lithospheric and sub-lithospheric mass distribution. The results can be better evaluated and interpreted if we can separate the effects of the two anomaly sources, which will be future work.

**Supplementary Information** The online version contains supplementary material available at <https://doi.org/10.1007/s10712-023-09810-y>.

**Acknowledgements** We thank three anonymous reviewers for their constructive comments. This research is supported by the National Natural Science Foundation of China (Grant Nos. 42074109, 42204067). The authors thank the High Performance Computing Center of Central South University for support.

**Data availability** The data and codes used for this study are available in the Figshare repository (Chen et al. 2022) via <https://doi.org/10.6084/m9.figshare.20365548> with the CC BY 4.0 open-source license. The gravity field model EIGEN-6C4 (Ince et al. 2019) can be assessed from the International Centre for Global Earth Models (<http://icgem.gfz-potsdam.de/home>). The topography/bathymetry model ETOPO1 is available at <https://www.ngdc.noaa.gov/mgg/global/global.html>. The CRUST1.0 is available at <https://igppweb.ucsd.edu/~gabi/crust1.html>. The global lithospheric thickness model CAM2016 (Priestley et al. 2019) is available at <http://ds.iris.edu/ds/products/emc-cam2016/>. The average global seismic models (Hosseini et al. 2018) are available at <https://www.earth.ox.ac.uk/~smachine/cgi/>. The Moho depth and average crystalline crust P-wave velocity model are available by the reference (Szwilius et al. 2019).

## Declarations

**Conflict of interest** The authors have no competing interests to declare relevant to this article's content. All authors certify that they have no affiliations with or involvement in any organization or entity with any financial or non-financial interest in the subject matter or materials discussed in this manuscript. The authors have no financial or proprietary interests in any material discussed in this article.

## References

Agard P, Omrani J, Jolivet L, Whitechurch H, Vrielynck B, Spakman W, Monié P, Meyer B, Wortel R (2011) Zagros orogeny: a subduction-dominated process. *Geol Mag* 148:692–725



- Amante C, Eakins BW (2009) ETOPO1 1 arc-minute global relief model: procedures, data sources and analysis. NOAA Technical Memorandum NESDIS NGDC-24. National Geophysical Data Center, NOAA
- An M, Shi Y (2006) Lithospheric thickness of the Chinese continent. *Phys Earth Planet* 159:257–266
- Anderson EG (1976) The effect of topography on solutions of Stokes' problem. School of Surveying, University of New South Wales, Kensington
- Artemieva IM (2006) Global  $1^{\circ} \times 1^{\circ}$  thermal model TC1 for the continental lithosphere: implications for lithosphere secular evolution. *Tectonophysics* 416:245–277
- Artemieva IM (2019) Lithosphere structure in Europe from thermal isostasy. *Earth Sci Rev* 188:454–468
- Artemieva IM, Mooney WD (2001) Thermal thickness and evolution of Precambrian lithosphere: a global study. *J Geophys Res Solid Earth* 106:16387–16414
- Artemieva IM, Thybo H (2013) EUNASEIS: a seismic model for Moho and crustal structure in Europe, Greenland, and the North Atlantic region. *Tectonophysics* 609:97–153
- Artemieva IM, Thybo H, Cherepanova Y (2019) Isopycnicity of cratonic mantle restricted to kimberlite provinces. *Earth Planet Sci Lett* 505:13–19
- Artemjev ME, Kaban MK, Kucherinenko VA, Demyanov GV, Taranov VA (1994) Subcrustal density inhomogeneities of Northern Eurasia as derived from the gravity data and isostatic models of the lithosphere. *Tectonophysics* 240:249–280
- Asgharzadeh MF, von Frese RRB, Kim HR, Leftwich TE, Kim JW (2007) Spherical prism gravity effects by Gauss-Legendre quadrature integration. *Geophys J Int* 169:1–11
- Barth MG, Rudnick RL, Horn I, McDonough WF, Spicuzza MJ, Valley JW, Haggerty SE (2002) Geochemistry of xenolithic eclogites from West Africa, part 2: origins of the high MgO eclogites. *Geochim Cosmochim Acta* 66:4325–4345
- Barthelmes F (2013) Definition of functionals of the geopotential and their calculation from spherical harmonic models: theory and formulas used by the calculation service of the International Centre for Global Earth Models (ICGEM). Scientific Technical Report 09/02, revised Edition, <http://icgem.gfz-potsdam.de/ICGEM/>, Deutsches GeoForschungsZentrum GFZ, Potsdam
- Becker TW, Faccenna C, Humphreys ED, Lowry AR, Miller MS (2014) Static and dynamic support of western United States topography. *Earth Planet Sci Lett* 402:234–246
- Becker TW, Lowry AR, Faccenna C, Schmandt B, Borsa A, Yu C (2015) Western US intermountain seismicity caused by changes in upper mantle flow. *Nature* 524:458
- Behn MD, Boettcher MS, Hirth G (2007) Thermal structure of oceanic transform faults. *Geology* 35:307–310
- Bonatti E (1985) Punctiform initiation of seafloor spreading in the Red Sea during transition from a continental to an oceanic rift. *Nature* 316:33–37
- Buehler J, Shearer P (2017) Uppermost mantle seismic velocity structure beneath USArray. *J Geophys Res Solid Earth* 122:436–448
- Chang SJ, Merino M, Van der Lee S, Stein S, Stein CA (2011) Mantle flow beneath Arabia offset from the opening Red Sea. *Geophys Res Lett* 38 L04301
- Chang SJ, Van Der Lee S, Flanagan MP, Bedle H, Marone F, Matzel EM, Pasyanos ME, Rodgers AJ, Romanowicz B, Schmid C (2010) Joint inversion for three-dimensional S velocity mantle structure along the Tethyan margin. *J Geophys Res Solid Earth* 115 B08309
- Chen B, Zhao G, Kaban MK, Du J, Liu J (2022) Dataset for the crust and mantle gravity disturbances and their implications. *figshare*. Dataset
- Chen M, Niu F, Tromp J, Lenardic A, Lee CA, Cao W, Ribeiro J (2017) Lithospheric foundering and underthrusting imaged beneath Tibet. *Nat Commun* 8:15659
- Cherepanova Y, Artemieva I (2015) Density heterogeneity of the cratonic lithosphere: a case study of the Siberian Craton. *Gondwana Res* 28:1344–1360
- Cherepanova Y, Artemieva IM (2013) Subsidence of the West Siberian Basin: geophysical evidence for eclogitization. EGU General Assembly Conference Abstracts, pp EGU2013–7031
- Cherepanova Y, Artemieva IM, Thybo H, Chemia Z (2013) Crustal structure of the Siberian craton and the West Siberian basin: an appraisal of existing seismic data. *Tectonophysics* 609:154–183
- Christensen NI, Mooney WD (1995) Seismic velocity structure and composition of the continental crust: a global view. *J Geophys Res Solid Earth* 100:9761–9788
- Claessens SJ, Hirt C (2013) Ellipsoidal topographic potential: new solutions for spectral forward gravity modeling of topography with respect to a reference ellipsoid. *J Geophys Res Solid Earth* 118:5991–6002
- Clouzet P, Masson Y, Romanowicz B (2018) Box tomography: first application to the imaging of upper-mantle shear velocity and radial anisotropy structure beneath the North American continent. *Geophys J Int* 213:1849–1875
- Davies JH (2013) Global map of solid Earth surface heat flow. *Geochem Geophys Geosyst* 14:4608–4622

- Deng Y, Levandowski W, Kusky T (2017) Lithospheric density structure beneath the Tarim basin and surroundings, northwestern China, from the joint inversion of gravity and topography. *Earth Planet Sci Lett* 460:244–254
- Deng Y, Zhang Z, Badal J, Fan W (2014) 3-D density structure under South China constrained by seismic velocity and gravity data. *Tectonophysics* 627:159–170
- Eakin CM, Rychert CA, Harmon N (2018) The role of oceanic transform faults in seafloor spreading: a global perspective from seismic anisotropy. *J Geophys Res Solid Earth* 123:1736–1751
- El-Sharkawy A, Meier T, Lebedev S, Behrmann JH, Hamada M, Cristiano L, Weidle C, Köhn D (2020) The slab puzzle of the Alpine-Mediterranean region: insights from a new, high-resolution, shear wave velocity model of the upper mantle. *Geochem Geophys Geosyst* 21:e2020GC008993
- Faccenna C, Becker TW (2010) Shaping mobile belts by small-scale convection. *Nature* 465:602–605
- Faccenna C, Becker TW (2020) Topographic expressions of mantle dynamics in the Mediterranean. *Earth Sci Rev* 209:103327
- Faccenna C, Becker TW, Auer L, Billi A, Boschi L, Brun JP, Capitanio FA, Funicello F, Horvath F, Jolivet L (2014) Mantle dynamics in the Mediterranean. *Rev Geophys* 52:283–332
- Faccenna C, Becker TW, Jolivet L, Keskin M (2013) Mantle convection in the Middle East: reconciling Afar upwelling, Arabia indentation and Aegean trench rollback. *Earth Planet Sci Lett* 375:254–269
- Faul UH, Jackson I (2005) The seismological signature of temperature and grain size variations in the upper mantle. *Earth Planet Sci Lett* 234:119–134
- Finger NP, Kaban MK, Tesauro M, Haeger C, Mooney WD, Thomas M (2021) A thermo-compositional model of the cratonic lithosphere of South America. *Geochem Geophys Geosyst* 22:e2020GC009307
- Finger NP, Kaban MK, Tesauro M, Mooney WD, Thomas M (2022) A thermo-compositional model of the African cratonic lithosphere. *Geochem Geophys Geosyst* 23:e2021GC010296
- Furlong KP, Chapman DS (2013) Heat flow, heat generation, and the thermal state of the lithosphere. *Annu Rev Earth Planet Sci* 41:385–410
- Gee DG, Stephenson RA (2006) The European lithosphere: an introduction. In: Gee DG, Stephenson RA (Eds.) *European Lithosphere Dynamics*. The Geological Society of London, London, pp 1–9
- Goes S (2002) Thermal structure of the North American uppermost mantle inferred from seismic tomography. *J Geophys Res* 107:ETG-2
- Gómez-García ÁM, Meeßen C, Scheck-Wenderoth M, Monsalve G, Bott J, Bernhardt A, Bernal G (2019) 3-D modeling of vertical gravity gradients and the delimitation of tectonic boundaries: the caribbean oceanic domain as a case study. *Geochem Geophys Geosyst* 20:5371–5393
- Griffin W, O'Reilly S, Abe N, Aulbach S, Davies R, Pearson N, Doyle B, Kivi K (2003) The origin and evolution of Archean lithospheric mantle. *Precamb Res* 127:19–41
- Grombein T, Seitz K, Heck B (2013) Optimized formulas for the gravitational field of a tesseroid. *J Geod* 87:645–660
- Grombein T, Seitz K, Heck B (2014) Topographic–isostatic reduction of GOCE gravity gradients, earth on the edge: science for a sustainable planet. Springer, Berlin, pp 349–356
- Grombein T, Seitz K, Heck B (2016) The rock–water–ice topographic gravity field model RWI\_TOPO\_2015 and its comparison to a conventional rock-equivalent version. *Surv Geophys* 37:937–976
- Haeger C, Kaban MK, Tesauro M, Petrunin AG, Mooney WD (2019) 3-D density, thermal, and compositional model of the antarctic lithosphere and implications for its evolution. *Geochem Geophys Geosyst* 20:688–707
- Heck B, Seitz K (2007) A comparison of the tesseroid, prism and point-mass approaches for mass reductions in gravity field modelling. *J Geod* 81:121–136
- Herceg M, Artemieva IM, Thybo H (2016) Sensitivity analysis of crustal correction for calculation of lithospheric mantle density from gravity data. *Geophys J Int* 204:687–696
- Hirt C, Yang M, Kuhn M, Bucha B, Kurzmann A, Pail R (2019) SRTM2gravity: an ultrahigh resolution global model of gravimetric terrain corrections. *Geophys Res Lett* 46:4618–4627
- Hoernle K, Zhang Y-S, Graham D (1995) Seismic and geochemical evidence for large-scale mantle upwelling beneath the eastern Atlantic and western and central Europe. *Nature* 374:34–39
- Hofmann-Wellenhof B, Moritz H (2006) *Physical geodesy*. Springer, Berlin
- Holt PJ, van Hunen J, Allen MB (2012) Subsidence of the West Siberian Basin: effects of a mantle plume impact. *Geology* 40:703–706
- Hosseini K, Matthews KJ, Sigloch K, Shephard GE, Domeier M, Tsekhmistrenko M (2018) SubMachine: web-based tools for exploring seismic tomography and other models of earth's deep interior. *Geochem Geophys Geosyst* 19:1464–1483
- Huang Z, Zhao D (2022) Seismotectonics of Mongolia and Baikal rift zone controlled by lithospheric structures. *Geophys Res Lett* 49:e2022GL099525

- Hyndman R, Currie C (2011) Why is the North America Cordillera high? Hot backarcs, thermal isostasy, and mountain belts. *Geology* 39:783–786
- Hyndman R, Lewis T (1999) Geophysical consequences of the Cordillera-Craton thermal transition in southwestern Canada. *Tectonophysics* 306:397–422
- Ince ES, Barthelmes F, Reißland S, Elger K, Förste C, Flechtner F, Schuh H (2019) ICGEM—15 years of successful collection and distribution of global gravitational models, associated services, and future plans. *Earth Syst Sci Data* 11:647–674
- Jolivet L, Faccenna C (2000) Mediterranean extension and the Africa-Eurasia collision. *Tectonics* 19:1095–1106
- Jordan TH (1978) Composition and development of the continental tectosphere. *Nature* 274:544–548
- Kaban MK, El Khrepy S, Al-Arifi N, Tesauro M, Stolk W (2016a) Three-dimensional density model of the upper mantle in the Middle East: interaction of diverse tectonic processes. *J Geophys Res Solid Earth* 121:5349–5364
- Kaban MK, Mooney WD, Petrunin AG (2015) Cratonic root beneath North America shifted by basal drag from the convecting mantle. *Nat Geosci* 8:797–800
- Kaban MK, Schwintzer P, Artemieva IM, Mooney WD (2003) Density of the continental roots: compositional and thermal contributions. *Earth Planet Sci Lett* 209:53–69
- Kaban MK, Schwintzer P, Tikhotsky SA (1999) A global isostatic gravity model of the Earth. *Geophys J Int* 136:519–536
- Kaban MK, Sidorov RV, Soloviev AA, Gvishiani AD, Petrunin AG, Petrov OV, Kashubin SN, Androsov EA, Milshtein ED (2022) A new Moho map for North-Eastern Eurasia based on the analysis of various geophysical data. *Pure Appl Geophys* 179:3903–3916c
- Kaban MK, Stolk W, Tesauro M, El Khrepy S, Al-Arifi N, Beekman F, Cloetingh SAPL (2016b) 3D density model of the upper mantle of Asia based on inversion of gravity and seismic tomography data. *Geochem Geophys Geosyst* 17:4457–4477
- Kaban MK, Tesauro M, Cloetingh S (2010) An integrated gravity model for Europe's crust and upper mantle. *Earth Planet Sci Lett* 296:195–209
- Kaban MK, Tesauro M, Mooney WD, Cloetingh SA (2014) Density, temperature, and composition of the North American lithosphere—New insights from a joint analysis of seismic, gravity, and mineral physics data: 1. Density structure of the crust and upper mantle. *Geochem Geophys Geosyst* 15:4781–4807
- Ke X, Tian M, Guan D, Wang Y, Shi H (2019) Gravitational gradients derived from GOCE and density structures beneath the North China Craton. *J Asian Earth Sci* 174:152–166
- Kind R, Yuan X (2010) Geophysics. Seismic images of the biggest crash on Earth. *Science* 329:1479–1480
- Koulakov I, Bushenkova N (2010) Upper mantle structure beneath the Siberian craton and surrounding areas based on regional tomographic inversion of P and PP travel times. *Tectonophysics* 486:81–100
- Laske G, Masters G, Ma Z, Pasyanos M (2013) Update on CRUST1. 0-A 1-degree global model of Earth's crust. *Geophys Res Abstr* 15 abstrEGU2013-2658
- Lebedev S, Meier T, van der Hilst RD (2006) Asthenospheric flow and origin of volcanism in the Baikal Rift area. *Earth Planet Sci Lett* 249:415–424
- Lee C-TA, Luffi P, Chin EJ (2011) Building and destroying continental mantle. *Annu Rev Earth Planet Sci* 39:59–90
- Lei J (2011) Seismic tomographic imaging of the crust and upper mantle under the central and western Tien Shan orogenic belt. *J Geophys Res* 116 B09305
- Lei J, Zhao D (2007) Teleseismic P-wave tomography and the upper mantle structure of the central Tien Shan orogenic belt. *Phys Earth Planet Lett* 162:165–185
- Li C, van der Hilst RD, Meltzer AS, Engdahl ER (2008) Subduction of the Indian lithosphere beneath the Tibetan Plateau and Burma. *Earth Planet Sci Lett* 274:157–168
- Li J, Ding W, Lin J, Xu Y, Kong F, Li S, Huang X, Zhou Z (2021) Dynamic processes of the curved subduction system in Southeast Asia: a review and future perspective. *Earth Sci Rev* 217:103647
- Liang Q, Chen C, Kaban MK, Thomas M (2019) Upper-mantle density structure in the Philippine Sea and adjacent region and its relation to tectonics. *Geophys J Int* 219:945–957
- Liang Q, Chen C, Li Y (2014) 3-D inversion of gravity data in spherical coordinates with application to the GRAIL data. *J Geophys Res Planets* 119:1359–1373
- Matthews KJ, Maloney KT, Zahirovic S, Williams SE, Seton M, Mueller RD (2016) Global plate boundary evolution and kinematics since the late Paleozoic. *Global Planet Change* 146:226–250
- Mooney WD (2015) Crust and lithospheric structure—global crustal structure. In: Schubert G (ed) *Treatise on geophysics*, 2nd edn. Elsevier, Amsterdam, pp 361–417
- Mooney WD, Kaban MK (2010) The North American upper mantle: density, composition, and evolution. *J Geophys Res Solid Earth* 115 B12424
- Mooney WD, Laske G, Masters TG (1998) CRUST 5.1: a global crustal model at 5×5. *J Geophys Res Solid Earth* 103:727–747

- Mooney WD, Vidale JE (2003) Thermal and chemical variations in subcrustal cratonic lithosphere: evidence from crustal isostasy. *Lithos* 71:185–193
- Morgan JP, Forsyth DW (1988) Three-dimensional flow and temperature perturbations due to a transform offset: effects on oceanic crustal and upper mantle structure. *J Geophys Res Solid Earth* 93:2955–2966
- Panet I, Pajot-Métivier G, Greff-Leffitz M, Métivier L, Diament M, Mandea M (2014) Mapping the mass distribution of Earth's mantle using satellite-derived gravity gradients. *Nat Geosci* 7:131–135
- Parsons T, Thompson GA, Sleep NH (1994) Mantle plume influence on the Neogene uplift and extension of the US western Cordillera? *Geology* 22:83–86
- Pasyanos ME, Masters TG, Laske G, Ma Z (2014) LITHO1.0: an updated crust and lithospheric model of the Earth. *J Geophys Res Solid Earth* 119:2153–2173
- Pearson D, Wittig N (2014) The formation and evolution of cratonic mantle lithosphere—evidence from mantle xenoliths. In: Holland HD, Turekian KK (eds) *Treatise on geochemistry*, 2nd edn. Elsevier, Amsterdam, pp 255–292
- Pearson DG, Scott JM, Liu J, Schaeffer A, Wang LH, van Hunen J, Szilas K, Chacko T, Kelemen PB (2021) Deep continental roots and cratons. *Nature* 596:199–210
- Petrov O, Morozov A, Shokalsky S, Kashubin S, Artemieva IM, Sobolev N, Petrov E, Ernst RE, Sergeev S, Smelror M (2016) Crustal structure and tectonic model of the Arctic region. *Earth Sci Rev* 154:29–71
- Pollack HN, Hurter SJ, Johnson JR (1993) Heat flow from the Earth's interior: analysis of the global data set. *Rev Geophys* 31:267–280
- Priestley K, McKenzie D (2006) The thermal structure of the lithosphere from shear wave velocities. *Earth Planet Sci Lett* 244:285–301
- Priestley K, McKenzie D, Ho T (2019) A lithosphere–asthenosphere boundary—a global model derived from multimode surface-wave tomography and petrology. In: Yuan H, Romanowicz B (eds) *Lithospheric discontinuities*, AGU Geophysical Monograph 239, pp 111–123
- Rexer M, Hirt C, Claessens S, Tenzer R (2016) Layer-based modelling of the earth's gravitational potential up to 10-km scale in spherical harmonics in spherical and ellipsoidal approximation. *Surv Geophys* 37:1035–1074
- Roecker S, Sabitova T, Vinnik L, Burmakov YA, Golvanov M, Mamatkanova R, Munirova L (1993) Three-dimensional elastic wave velocity structure of the western and central Tien Shan. *J Geophys Res Solid Earth* 98:15779–15795
- Root B, Novák P, Dirx D, Kaban M, van der Wal W, Vermeersen L (2016) On a spectral method for forward gravity field modelling. *J Geodyn* 97:22–30
- Root BC, Ebbing J, van der Wal W, England RW, Vermeersen LLA (2017) Comparing gravity-based to seismic-derived lithosphere densities: a case study of the British Isles and surrounding areas. *Geophys J Int* 208:1796–1810
- Saunders AD, England RW, Reichow MK, White RV (2005) A mantle plume origin for the Siberian traps: uplift and extension in the West Siberian Basin, Russia. *Lithos* 79:407–424
- Schaeffer A, Lebedev S (2014) Imaging the North American continent using waveform inversion of global and USArray data. *Earth Planet Sci Lett* 402:26–41
- Schaeffer AJ, Lebedev S (2013) Global shear speed structure of the upper mantle and transition zone. *Geophys J Int* 194:417–449
- Schivardi R, Morelli A (2011) EPmantle: a 3-D transversely isotropic model of the upper mantle under the European Plate. *Geophys J Int* 185:469–484
- Schutt D, Leshner C (2006) Effects of melt depletion on the density and seismic velocity of garnet and spinel lherzolite. *J Geophys Res Solid Earth* 111 B05401
- Shirey SB, Carlson RW, Richardson SH, Menzies A, Gurney JJ, Pearson DG, Harris JW, Wiechert U (2001) Archean emplacement of eclogitic components into the lithospheric mantle during formation of the Kaapvaal Craton. *Geophys Res Lett* 28:2509–2512
- Shulgin A, Artemieva IM (2019) Thermochemical heterogeneity and density of continental and oceanic upper mantle in the European-North atlantic region. *J Geophys Res Solid Earth* 124:9280–9312
- Steinberger B, Becker TW (2018) A comparison of lithospheric thickness models. *Tectonophysics* 746:325–338
- Stolk W, Kaban M, Beekman F, Tesauro M, Mooney WD, Cloetingh S (2013) High resolution regional crustal models from irregularly distributed data: application to Asia and adjacent areas. *Tectonophysics* 602:55–68
- Straume EO, Gaina C, Medvedev S, Hochmuth K, Gohl K, Whittaker JM, Fattah RA, Doornenbal JC, Hopper JR (2019) GlobSed: updated total sediment thickness in the world's oceans. *Geochem Geophys Geosyst* 20:1756–1772
- Sun Y, Dong S, Zhang H, Li H, Shi Y (2013) 3D thermal structure of the continental lithosphere beneath China and adjacent regions. *J Asian Earth Sci* 62:697–704
- Szwilius W, Afonso JC, Ebbing J, Mooney WD (2019) Global crustal thickness and velocity structure from geostatistical analysis of seismic data. *J Geophys Res Solid Earth* 124:1626–1652

- Tao K, Grand SP, Niu FL (2018) Seismic structure of the upper mantle beneath Eastern Asia from full waveform seismic tomography. *Geochem Geophys Geosyst* 19:2732–2763
- Tenzener R, Chen W (2019) Mantle and sub-lithosphere mantle gravity maps from the LITHO1.0 global lithospheric model. *Earth Sci Rev* 194:38–56
- Tenzener R, Chen W, Tsoulis D, Bagherbandi M, Sjöberg LE, Novák P, Jin S (2015) Analysis of the refined CRUST1.0 crustal model and its gravity field. *Surv Geophys* 36:139–165
- Tenzener R, Hamayun K, Vajda P (2009) Global maps of the CRUST 2.0 crustal components stripped gravity disturbances. *J Geophys Res Solid Earth* 114 B05408
- Tesauro M, Kaban MK, Aitken ARA (2020) Thermal and compositional anomalies of the Australian upper mantle from seismic and gravity data. *Geochem Geophys Geosyst* 21:e2020GC009305
- Tesauro M, Kaban MK, Mooney WD, Cloetingh S (2014a) NACr14: a 3D model for the crustal structure of the North American Continent. *Tectonophysics* 631:65–86
- Tesauro M, Kaban MK, Mooney WD, Cloetingh SA (2014b) Density, temperature, and composition of the North American lithosphere—New insights from a joint analysis of seismic, gravity, and mineral physics data: 2. Thermal and compositional model of the upper mantle. *Geochem Geophys Geosyst* 15:4808–4830
- Turcotte D, Schubert G (2014) *Geodynamics*, 3rd edn. Cambridge University Press, Cambridge
- Uieda L, Barbosa VCF, Braitenberg C (2016) Tesseroids: forward-modeling gravitational fields in spherical coordinates. *Geophysics* 81:F41–F48
- Vajda P, Ellmann A, Meurers B, Vaníček P, Novak P, Tenzer R (2008) Global ellipsoid-referenced topographic, bathymetric and stripping corrections to gravity disturbance. *Stud Geophys Geod* 52:19–34
- Van der Meer DG, Van Hinsbergen DJ, Spakman W (2018) Atlas of the underworld: slab remnants in the mantle, their sinking history, and a new outlook on lower mantle viscosity. *Tectonophysics* 723:309–448
- Wang Y (2001) Heat flow pattern and lateral variations of lithosphere strength in China mainland: constraints on active deformation. *Phys Earth Planet* 126:121–146
- Wang Y, Cao Z, Peng L, Liu L, Chen L, Lundstrom C, Peng D, Yang X (2023) Secular craton evolution due to cyclic deformation of underlying dense mantle lithosphere. *Nat Geosci* 16: 637–645
- Wang YY, Liu LJ, Zhou Q (2022a) Geoid reveals the density structure of cratonic lithosphere. *J Geophys Res-Sol Ea* 127:e2022JB024270
- Wang YY, Liu LJ, Zhou Q (2022b) Topography and gravity reveal denser cratonic lithospheric mantle than previously thought. *Geophys Res Lett* 49:e2021GL096844
- Wild-Pfeiffer F (2008) A comparison of different mass elements for use in gravity gradiometry. *J Geod* 82:637–653
- Xia B, Artemieva IM, Thybo H, Klemperer SL (2023) Strong Variability in the Thermal Structure of Tibetan Lithosphere Abstract Plain Language Summary Key Points. *J Geophys Res-Sol Ea* 128 e2022JB026213
- Zhao G, Chen B, Uieda L, Liu J, Kaban MK, Chen L, Guo R (2019) Efficient 3-D large-scale forward modeling and inversion of gravitational fields in spherical coordinates with application to lunar mascons. *J Geophys Res Solid Earth* 124:4157–4173
- Zhao GD, Liu JX, Chen B, Kaban MK, Du JS (2021) 3-D density structure of the lunar mascon basins revealed by a high-efficient gravity inversion of the GRAIL data. *J Geophys Res-Planet* 126:e2021JE006841
- Zhao W, Kumar P, Mechie J, Kind R, Meissner R, Wu Z, Shi D, Su H, Xue G, Karplus M, Tilmann F (2011) Tibetan plate overriding the Asian plate in central and northern Tibet. *Nat Geosci* 4:870–873
- Zhong YY, Ren ZY, Tang JT, Lin YF, Chen B, Deng YF, Jiang YD (2022) Constrained gravity inversion with adaptive inversion grid refinement in spherical coordinates and its application to mantle structure Beneath Tibetan Plateau. *J Geophys Res-Sol Ea* 127:e2021JB022916
- Zhu H, Bozdağ E, Tromp J (2015) Seismic structure of the European upper mantle based on adjoint tomography. *Geophys J Int* 201:18–52
- Zielhuis A, Nolet G (1994) Deep seismic expression of an ancient plate boundary in Europe. *Science* 265:79–81

**Publisher's Note** Springer Nature remains neutral with regard to jurisdictional claims in published maps and institutional affiliations.

Springer Nature or its licensor (e.g. a society or other partner) holds exclusive rights to this article under a publishing agreement with the author(s) or other rightsholder(s); author self-archiving of the accepted manuscript version of this article is solely governed by the terms of such publishing agreement and applicable law.

## Authors and Affiliations

Bo Chen<sup>1,2</sup>  · Mikhail K. Kaban<sup>3</sup> · Guangdong Zhao<sup>4</sup> · Jinsong Du<sup>5</sup> · Dawei Gao<sup>1,2</sup> 

✉ Dawei Gao  
daweigao@csu.edu.cn

<sup>1</sup> School of Geosciences and Info-Physics, Central South University, Changsha 410083, China

<sup>2</sup> Hunan Key Laboratory of Non-Ferrous Resources and Geological Hazard Detection, Changsha 410083, China

<sup>3</sup> GFZ German Research Centre for Geosciences, 14473 Telegrafenberg, Germany

<sup>4</sup> Key Laboratory of Earth Exploration and Information Technology of Ministry of Education, Chengdu University of Technology, Chengdu 610059, Sichuan, China

<sup>5</sup> Hubei Subsurface Multi-Scale Imaging Key Laboratory, School of Geophysics and Geomatics, China University of Geosciences, Wuhan 430074, China